Powder Technology 338 (2018) 519–537

Contents lists available at ScienceDirect

Powder Technology

journal homepage: www.elsevier.com/locate/powtec

Comprehensive multivariate sensitivity analysis of CFD-DEM simulations: Critical model parameters and their impact on fluidization hydrodynamics

A. Bakshi [a,b,*], M. Shahnam [b], A. Gel [b,c], T. Li [b], C. Altantzis [a,b], W. Rogers [b], A.F. Ghoniem [a]

[a] Massachusetts Institute of Technology, Cambridge, MA 02139, USA
[b] National Energy Technology Laboratory, Morgantown, WV 26507, USA
[c] ALPEMI Consulting, LLC, Phoenix, AZ 85044, USA

ARTICLE INFO

Article history:
Received 22 February 2018
Received in revised form 22 June 2018
Accepted 29 June 2018
Available online 17 July 2018

ABSTRACT

The development of CFD-DEM is critical for investigating particle phenomena and their coupling with reactor transport. However, there continues to be considerable uncertainty in the selection of model parameters because of limitations in: (a) experimental measurements of multi-particle interactions, and (b) computational resources which have restricted most numerical studies to 2D simulations, in very small-scale systems (<50k particles) and/or to local sensitivity analysis. The focus of this study is to identify critical model parameters in 3D CFD-DEM simulations of fluidized beds through multivariate sensitivity analysis and quantify their impact on hydrodynamics. Towards this end, thirteen model parameters are considered and the sampling design matrix is constructed using the Morris-One-At-a-Time (MOAT) screening method. 3D CFD-DEM simulations with almost 170,000 glass bead particles (0.4 mm diameter) are conducted in a small rectangular pulsating fluidized bed, selected because of its repeatable bubbling patterns. Detailed bubble and particle dynamics data from 250+ simulations show that: (a) choosing exceedingly low normal spring stiffness has strong implications on particle velocities; (b) the impact of all contact dissipation parameters (normal restitution, friction and tangential damping) is tightly coupled and sensitivity to any one hinges on the choices of others; and (c) the stability of bubble patterns is contingent on their choices and almost-ideal as well as extremely dissipative systems exhibit no patterns. In addition, by investigating particle dynamics inside and around bubbles, we derive a working expression for the optimal choice of spring stiffness. Overall, this first-of-its-kind analysis provides important guidelines for CFD-DEM model parameter selection and the statistical framework developed here provides a robust strategy for the fundamental investigation of other particle-scale phenomena and simulation-based reactor design and optimization.

CFD-DEM, gas-solid fluidization, pulsating reactor, multivariate sensitivity, linear spring-dashpot model, spring stiffness

1. Introduction

Gas-solid fluidized bed reactors are commonly used in a wide range of energy and chemical conversion processes because of their high heat and mass transfer rates, thermal homogeneity and feedstock flexibility [1]. Some of the most common applications include fluidized bed reactors for coal and biomass gasification, fluid catalytic cracking (FCC), chemical looping combustion, carbon capture, energy storage applications and polymerization reactors [2–4]. Designing and optimizing the performance of these reactors continue to be challenging because of several technical constraints and limited ability to run non-intrusive diagnostics in the harsh conditions these reactors often operate in. The development of credible Computational Fluid Dynamics (CFD) based modeling and simulations tools along with high performance computing resources is becoming increasingly valuable and popular tool for the design, optimization, reliability and safety studies of chemical-conversion systems.

There are several frameworks for modeling gas-solid flows with varying accuracy and computational cost depending on the physical fidelity to be achieved [5]. The most popular are the Eulerian-Eulerian and the Eulerian-Lagrangian models. The former, popularly referred to as continuum or multi-fluid models, represent particles collectively as

* Corresponding author at: Massachusetts Institute of Technology, Cambridge, MA 02139, USA.
E-mail address: abakshi@mit.edu (A. Bakshi).

https://doi.org/10.1016/j.powtec.2018.06.049
0032-5910/

Nomenclature

Common symbol definitions

d	diameter
δ	particle deformation
e	restitution coefficient
ε	volume fraction
f	frequency
k	spring stiffness
m	particle mass
μ	friction coefficient
μ^*	modified means of gradients
n	number
η	damping coefficient
ϕ	phase
σ	standard deviation of gradients
U	superficial gas velocity
x	lateral location

Common sub-scripts

b	bubble-phase
g	gas-phase
in	plenum inlet
mf	minimum fluidization
n	normal
p	particle
pd	post-distributor
rms	root mean square
s	solids-phase
t	tangential
w	particle-wall

inter-penetrating continua and the hydrodynamics are efficiently predicted by solving PDEs similar to the Navier-Stokes equations of single-phase fluid flows. While this representation makes simulating large-scale reactors computationally tractable, the application of this framework for complex particulate flows (e.g., mixing and segregation of polydisperse mixtures, chemical conversion, adhesion, catalysis and so on) continues to be challenging because the underlying physics are either not well understood or accurate constitutive equations accounting for unresolved particle-scale phenomena are not available.

The coupled CFD-Discrete Element Modeling (CFD-DEM) approach is useful because solid particles are individually tracked and their collisions and interactions are resolved. The biggest drawback is their exceedingly high demand for computational resources, as even small scale-systems have millions of particles and simulation time-steps are constrained by particle collision time-scales [6]. Nevertheless, their high physical resolution makes them ideal for (a) the fundamental investigation of particle-scale phenomena (e.g. [7–9]) and (b) providing datasets for the development of constitutive equations (and subgrid models) required by lower resolution approaches (e.g. [10, 11]). CFD-DEM has been employed in a wide range of multiphysics, multiscale applications such as fluidized beds [12–20], chemical conversion reactors [21–23], environmental flow applications [24–26] and so on.

All CFD-DEM frameworks can be broadly classified as either being hard-sphere or soft-sphere approaches, which differ in their modeling of collisions and particle (DEM) time-step. The hard-sphere approach is based on instantaneous, pair-wise collisions of particles and is very efficient for modeling extremely dilute systems. However, this approach does not model enduring contact between particles (see [27] and references therein). Towards more generalized and robust modeling of particulate transport, Cundall and Strack [28] proposed the soft-sphere approach in 1979. The overall premise of this framework is that multiple particles are allowed to overlap during contact and the net force is based on a parallel combination of spring and dashpot forces. Several models have been proposed which account for non-linearities in the force-schemes (notably, Hertzian based contact) and allow the use of artificially high time-steps for speeding-up simulations [29]. The majority of published literature continues to use the soft-sphere approach in its original manifestation, the linear spring dashpot (LSD) model, because of its simplicity, and reasonable accuracy for different applications [29, 30].

The LSD model computes the normal and tangential forces between two contacting particles using a parallel combination of spring (conservative) and dashpot (dissipative) representations. All particle collisions and interactions, between themselves and with the walls, are characterized by mechanical properties: spring stiffness and dashpot damping, alongwith Coulomb friction which determines the condition of slipping on contact. Despite significant advances in experimental techniques, there continues to be considerable uncertainty in the selection of appropriate model parameters in the LSD model because experimental measurements are possible only for simplified (binary) normal collisions, and estimating tangential interactions continues to be challenging [31]. The complexity is further compounded by the sensitivity of these parameters to material manufacturing properties such as surface roughness. It is not surprising that parametric estimation is often a model tuning exercise through numerical experiments and sensitivity analysis. Most investigations have focused on the spring stiffness (which directly impacts simulation time-step), normal restitution and/or friction coefficients [32–40] with different findings and conclusions. For instance, some studies conclude that friction and restitution have little influence on the hydrodynamics, as long as there is some route for energy dissipation [37, 39], while others show significant sensitivities [34, 40]. While they provide valuable insights into the fundamentals of particle interactions and their coupling with reactor-scale transport, majority of these sensitivity studies are limited to, at most, two model parameters and often with relatively low particle count (≤ 50,000) for computational tractability. Since parametric interactions are dynamic, non-linear and highly coupled, such an approach is susceptible to bias with regard to the nominal choices of other parameters. Similarly, for non-cohesive particles, the choice of spring stiffness is shown to have little impact on bubbling dynamics [41–43] while other studies indicate severe consequences on particle velocities [44, 45]. Although sensitivities (or the mere lack of) of numerical simulations to the underlying model parameters are often application-specific, these observations clearly demonstrate the need for considering multiple, independent dynamic metrics such as bubble characteristics and particle dynamics.

This study is part of a larger effort towards verification, validation and uncertainty quantification of multiphase flow simulations using the National Energy Technology Laboratory's open-source solver MFiX [46–49]. We focus on identifying critical CFD-DEM model parameters and their impact on the hydrodynamics in fluidized beds. A pulsating fluidized bed is selected as a test case because of its organized bubbling patterns. In these reactors, the oscillation in superficial gas flow can significantly improve the fluidization quality and mass transfer by controlling bubble formation and rise precisely [50–53]. Flow patterns in these reactors have been subject to several numerical investigations using both the Eulerian (e.g. [54, 55]) and CFD-DEM frameworks (e.g. [56–58]). Coppens et al. [59] reported that homogeneous fluidization conditions are most favorable for creating repeatable bubbling patterns. Through their experiments in a pseudo-2D pulsating fluidized bed, Coppens and van Ommen [60] observed regular, periodic bubble patterns as manifestations of the fluid drag and particle frictional interactions. These features are absent in continuum (Two-Fluid Model) simulations [61, 62] but have been successfully reproduced in

CFD-DEM simulations [63, 64]. Overall, since pulsating fluidized beds dynamically oscillate between bubbling and granular-relaxation dominated regimes, and produce repeatable bubbling patterns, they offer excellent opportunity for the investigation and validation of CFD-DEM simulations.

Numerical experiments are carried out on a lab-scale thin rectangular fluidized bed with cross-sectional area 5.0×0.5 cm ^{2} which accommodates approximately 170,000 glass bead particles (0.4 mm diameter). The operating conditions, i.e. mean, amplitude and frequency of inlet gas flow, are chosen so that repeatable, alternating bubbling patterns are observed (see Fig. 2). This setup is suitable for detailed CFD-DEM study, parametric analysis as well as experimental measurements in the laboratory. Uncertain CFD-DEM model parameters are identified based on rigorous literature survey and feedback from NETL. In order to assess the significance of these parameters systematically, we consider a simulation matrix by employing statistical-design-of-experiments with the aid of PSUADE (Problem Solving environment for Uncertainty Analysis and Design Exploration), the open source toolkit by Lawrence Livermore National Laboratory for uncertainty quantification analysis. Next, 3D CFD-DEM simulations are conducted for 40s of real time and all relevant data is processed at 50 Hz frequency for bubble statistics using MS3DATA (Multiphase-flow Statistics using 3D Detection and Tracking Algorithm) [65] and particle field metrics. Finally, the quantities of interest (Qols) from all simulations are aggregated for statistical analysis using PSUADE and MATLAB scripts. More than 250 3D CFD-DEM simulations are conducted, typically over 10–30 days on 40–80 cores each, making this one of the most rigorous statistical analysis of dense-phase particulate flows. Note that this study is focused on identifying critical model parameters (among many uncertain ones) based on the ability of CFD-DEM simulations to predict repeatable, alternating bubble patterns which are observed under identical operating conditions in pulsating fluidized beds. Direct, quantitative comparison of simulations with experimental data is not presented here and will be discussed in subsequent studies focused on validation (and calibration) of critical parameters identified here.

In the following sections, the hydrodynamic model is first discussed in Section 2, followed by a brief description of the statistical tools and uncertain model parameters in Section 3. Section 4 details the simulation setup and solver details and all related post-processing is described in Section 5. Finally, results from sensitivity analyses along with detailed investigation regarding the role of the identified critical parameters (normal spring stiffness, restitution, friction and tangential damping) are presented in Section 6.

2. Hydrodynamic model

The pulsating fluidized bed is simulated using MFiX version 2016–1 [66], NETL's open-source solver for simulating gas-solid flows. In MFIX-DEM, the gas-phase is treated as a continuum using the Eulerian framework, similar to traditional single-phase CFD, while the solid-phase is modeled using discrete particles in a Lagrangian framework.

2.1. Gas-phase

The continuity and momentum equations, in the absence of phase-change and chemical reactions are:

$$\frac{\partial\left(\varepsilon_g\rho_g\right)}{\partial t}+\nabla\cdot\left(\varepsilon_g\rho_g\boldsymbol{V}_g\right)=0 \tag{1}$$

$$\frac{D}{Dt}\left(\varepsilon_g\rho_g\boldsymbol{V}_g\right)=-\varepsilon_g\nabla p-\nabla\cdot\left(\varepsilon_g\bar{\bar{\boldsymbol{\tau}}}_g\right)-S_p+\varepsilon_g\rho_g\mathbf{g} \tag{2}$$

where ε_g, ρ_g, $\boldsymbol{V}_g$ and P_g are the gas-phase volume fraction, density, velocity vector and pressure (in the fluid grid cell), and $\mathbf{g}$ is the acceleration due to gravity. Similar to single-phase CFD, the stress tensor $\bar{\bar{\boldsymbol{\tau}}}_g$ is computed as

$$\bar{\bar{\boldsymbol{\tau}}}_g=-\left[2\mu_g\bar{\bar{\mathbf{D}}}_g+\left(\lambda_g-\frac{2}{3}\mu_g\right)\left(\nabla\cdot\boldsymbol{V}_g\right)\bar{\bar{\mathbf{I}}}\right] \tag{3}$$

where $\bar{\bar{\mathbf{D}}}_g=\frac{1}{2}\left[\nabla\boldsymbol{V}_g+\left(\nabla\boldsymbol{V}_g\right)^T\right]$ is the strain rate tensor and μ_g and λ_g are the dynamic and second coefficients of gas-phase viscosity. S_p represents the momentum exchange between the gas and particles, and is modeled as

$$S_p=\frac{1}{\forall_{cell}}\sum\frac{\beta^i\forall_p}{\varepsilon_s}\left(\boldsymbol{V}_g\left(\boldsymbol{X}^i\right)-\boldsymbol{V}^i\right) \tag{4}$$

where β^i is the momentum transfer coefficient (defined later) between gas and particle i, $\boldsymbol{X}^i$ is the particle location vector and ε_s is the volume averaged packing fraction. $\forall_p$ and $\forall_{cell}$ are the geometric volumes of the particle and grid cell, respectively.

2.2. Solid-phase: Discrete element method (DEM)

For a mono-disperse system, the position, linear and angular velocities of the i^{th} particle evolve according to Newton's second laws as:

$$\frac{d\boldsymbol{X}^i}{dt}=\boldsymbol{V}^i \tag{5}$$

$$m\frac{d\boldsymbol{V}^i}{dt}=m\mathbf{g}+\mathbf{F}_d^i+\mathbf{F}_c^i$$

$$I\frac{d\boldsymbol{\omega}^i}{dt}=\boldsymbol{\tau}^i$$

where m and I are the mass and moment of inertia of each particle. $\mathbf{F}_d^i$ is the total drag force (pressure and viscous), $\mathbf{F}_c^i$ is the net contact force (interaction with other particles) and $\boldsymbol{\tau}^i$ is the sum of all torques acting on the i^{th} particle.

The contact force between two particles i and j is based on the Linear Spring and Dashpot (LSD) model proposed by Cundall and Strack [28]. In this approach, both the normal and tangential contact forces are comprised of linear spring (conservative) and dashpot (dissipative) components. The total normal force is given by

$$\mathbf{F_n^{i,j}}=\mathbf{F_{n,S}^{i,j}}+\mathbf{F_{n,D}^{i,j}}=-k_n\delta_n\boldsymbol{\xi}_\mathbf{n}-\eta_n\mathbf{V_n^{i,j}} \tag{6}$$

where k_n is the spring stiffness, η_n is the dashpot damping, δ_n is the overlap between two particles, $\boldsymbol{\xi}_\mathbf{n}$ is the normal unit vector along the particle radius and $\mathbf{V_n^{i,j}}$ is the normal component of the impact velocity

$$\mathbf{V_n^{i,j}}=\left(\mathbf{V^{i,j}}\cdot\boldsymbol{\xi}_\mathbf{n}\right)\boldsymbol{\xi}_\mathbf{n} \tag{7}$$

The normal collision of two particles can be solved analytically (with initial conditions $\delta_n(t=0)=0$ and $\dot{\delta}_n(t=0)=V_{n0}$), and the collision time t_{col} and maximum overlap δ_{max} are related to k_n and normal restitution e_n through [32]

$$t_{col}=\sqrt{\frac{m_e}{k_n}}\sqrt{\pi^2+ln^2e_n} \tag{8}$$

$$\delta_{max}=V_{n0}\sqrt{\frac{m_e}{k_n}}\,exp\left(-\frac{arctan(\pi/\ \ln e_n)}{(\pi/\ \ln e_n)}\right) \tag{9}$$

where m_e is the effective mass given by $(1/m_i+1/m_j)^{-1}$. η_n is also adjusted based on t_{col} so that restitution e_n is recovered after the

particles rebound:

$$\eta_n = -\frac{2\sqrt{m_e k_n}\,|\ln e_n|}{\sqrt{\pi^2 + \ln^2 e_n}} \tag{10}$$

Note that both t_{col} and δ_{max} increase as k_n is reduced. While useful for speeding-up simulations (particle collisions can be resolved in larger time-steps), very low values of k_n can result in excessive particle overlap which has severe implications on the bed hydrodynamics. This will be discussed later in Section 6.3. Meanwhile, the tangential force is modeled in a similar way (in terms of tangential spring stiffness k_t and damping coefficient η_t), with the added condition of slip/no-slip imposed by Coulomb friction, i.e.

$$\mathbf{F_t^{i,j}} = \begin{cases} -k_t\delta_t - \eta_t \mathbf{V_t^{i,j}} & \text{if } \mathbf{F_t^{i,j}} \le \mu\left|\mathbf{F_{n,S}^{i,j}}\right| \\ -\mu\left|\mathbf{F_{n,S}^{i,j}}\right|\boldsymbol{\xi_t} & \text{otherwise} \end{cases} \tag{11}$$

where μ is the friction (kinetic) coefficient, $\boldsymbol{\xi_t}$ is the tangential unit vector and the total tangential overlap δ_t (after the start of contact at t_0) is computed using

$$\delta_t = \int_{t_0}^{t} \left(\mathbf{V^{i,j}} - \mathbf{V_n^{i,j}}\right)\cdot \boldsymbol{\xi_t}\, dt \tag{12}$$

In order to prevent unphysical elongation of tangential spring, the tangential overlap is frozen at $|\mathbf{F_{n,S}^{i,j}}|\boldsymbol{\xi_t}/k_t$ during frictional slip [67].

The tangential component of contact force also generates torque on the i^{th} particle that is given by

$$\boldsymbol{\tau^{i,j}} = \mathrm{L}^i \boldsymbol{\xi_n} \times \mathbf{F_t^{i,j}} \tag{13}$$

where L^i is the distance from the particle center to the contact point. Finally, the total drag force $\mathbf{F_d^i}$ is:

$$\mathbf{F_d^i} = -\nabla P_g\left(\mathbf{X^i}\right)\forall^i + \frac{\beta^i \forall^i}{\varepsilon^i}\left(\mathbf{V_g}\left(\mathbf{X^i}\right) - \mathbf{V^i}\right) \tag{14}$$

where $P_g(\mathbf{X^i})$ is the average gas phase pressure at the particle location $\mathbf{X^i}$. In this study, the drag coefficient β^i is calculated using the Gidaspow model [68] which combines the Ergun and Wen-Yu equations for pressure drop in fixed and homogeneously fluidized beds, respectively:

$$\beta^i = \begin{cases} 150\ \dfrac{\varepsilon_s^2 \mu_g}{\varepsilon_g (d\phi)^2} + 1.75\ \dfrac{\varepsilon_s \rho_g \left|\mathbf{V_g}\left(\mathbf{X^i}\right) - \mathbf{V^i}\right|}{d\phi} & \text{if } \varepsilon_g < 0.8 \\ \dfrac{3}{4} C_d^i\ \dfrac{\varepsilon_s \varepsilon_g^{-1.65} \rho_g \left|\mathbf{V_g}\left(\mathbf{X^i}\right) - \mathbf{V^i}\right|}{d\phi} & \text{if } \varepsilon_g \ge 0.8 \end{cases} \tag{15}$$

$$C_d^i = \begin{cases} \dfrac{24}{Re^i \varepsilon_g}\left(1 + 0.15\left(Re^i \varepsilon_g\right)^{0.687}\right) & \text{if } Re^i \varepsilon_g < 1000 \\ 0.44 & \text{if } Re^i \varepsilon_g \ge 1000 \end{cases}$$

$$Re^i = \frac{\rho_g \left|\mathbf{V_g}\left(\mathbf{X^i}\right) - \mathbf{V^i}\right| d\phi}{\mu_g}$$

where ϕ is the particle sphericity. Further details on the governing equations and their implementation in MFiX-DEM can be found in [69, 70].

3. Statistical screening study for identifying influential parameters among many

Sensitivity analysis conducted in this study is based on the non-intrusive uncertainty quantification technique i.e. the simulation software is treated as a black box and UQ analysis is conducted by sampling simulations using random or deterministic strategies. Such an approach is particularly beneficial for complex computational models because reformulations of the governing equations and/or structural changes within the code are not required. For the screening study of CFD-DEM model parameters, the MOAT method is employed because of its high efficiency for screening sensitive parameters, which is particularly desirable when sample evaluations are expensive. This method is described mathematically in Section 3.1, followed by a brief survey of uncertain parameters in Section 3.2 and modeling assumptions in Section 3.3.

3.1. MOAT analysis

Several approaches for sensitivity analysis have been proposed in the literature. Quantitative methods typically decompose output variance into contributions of all input factors, making use of correlation ratios, response surfaces, etc., but are often computationally expensive if more than a few uncertain parameters are considered. On the other hand, qualitative methods heuristically score the relative sensitivities of parameters but do not provide quantitative description of absolute sensitivities [71]. This lack of higher fidelity, though, makes them computationally more efficient and often the preferred method for parameter screening studies in complex systems with expensive simulations (such as CFD-DEM) and where more than few parameters are under consideration.

Some of the commonly used screening methods are Correlation Analysis (CA) Morris-One-At-a-Time (MOAT), Multivariate Adaptive Regression Splines (MARS) and Sum-Of-Trees (SOT) (see [71] and references therein), with different sampling techniques and overall suitability (e.g. some methods are apt for screening sensitive parameters while others identify insensitive ones). In this study, we employ the MOAT method [72, 73] because of its lower computational burden [71] and successful application to complex non-linear systems such as ecological models [73–77], building energy [78, 79] and traffic flow [80, 81] simulations.

The guiding principle of MOAT analysis is that the most influential input parameters (or *factors*) can be identified based on two sensitivity metrics: μ, which quantifies the overall influence of a factor on simulation output and σ, which characterizes its higher order effects i.e. non-linearity and coupled interactions with other factors. Each factor p_i, $i = 1, \ldots, n$ is discretized at l selected levels forming an n-dimensional l-level grid Ω for numerical experimentation. The first sample is chosen randomly and each subsequent sample is picked changing one-factor-at-a-time (*random walk*), so that the elementary effect F_i of factor p_i is defined as

$$F_i \sim d_i(\boldsymbol{X}) = \frac{y(\boldsymbol{X} + \boldsymbol{e_i}\Delta) - y(\boldsymbol{X})}{\Delta} \tag{16}$$

$$\boldsymbol{X} = X_1, \ldots, X_{i-1}, X_i, X_{i+1}, \ldots, X_n$$

$$\boldsymbol{X} + \boldsymbol{e_i}\Delta = X_1, \ldots, X_{i-1}, X_i + \Delta, X_{i+1}, \ldots, X_n$$

where $\boldsymbol{X}$ represents coordinates of an arbitrary sample in the parametric space, y is the quantity (metric) of interest, $\boldsymbol{e_i}$ is the unit vector along the i^{th} direction and Δ is chosen from $[1/(l-1), \ldots 1 - 1/(l-1)]$ so that both $\boldsymbol{X}$ and $\boldsymbol{X} + \boldsymbol{e_i}\Delta$ are still within Ω. Therefore, a trajectory of $n+1$ sampled points, also called a replication, is required to quantify elementary effects of n factors. Since this approach does not guarantee equal-probability sampling from Ω, Morris suggested the use of

r trajectories and evaluating the sensitivity measures μ_i and σ_i as the average and standard deviation of the distribution of F_i. In this study, the modified mean μ^* proposed by Campolongo et al. 2007 [73] is used which accounts for absolute elementary effects, i.e.

$$d_i(\boldsymbol{X}) = \left|\frac{y(\mathbf{X}+\mathbf{e_i}\Delta)-y(\mathbf{X})}{\Delta}\right| \quad (17)$$

in order to prevent opposing signs of gradients in the calculation of μ^*. As is typical in sensitivity analyses, uncertain inputs are assumed to be distributed uniformly in [0,1] interval, i.e., all possible values have equal probability and then transformed to their actual ranges. $l = 4$ and $\Delta = 2/3$ are chosen to ensure certain symmetric treatment of inputs, while r is decided based on the statistical convergence of parametric rankings (discussed later in Section 6.2). More details regarding this approach can be found in [72, 73].

3.2. Uncertain model input parameters

Model parameters considered uncertain in this study are listed in Table 1. Choices for their nominal and range values (i.e., lower and upper bounds) are based on commonly reported values in the literature and feedback from domain experts at NETL. Note that in addition to physical model parameters, model-specific numerical parameters (P_{11}—P_{13}) are also considered in order to evaluate their impact on bubbling patterns and potentially reduce computational cost of 3D CFD-DEM simulations for subsequent validation studies. For numerical experimentation, all parameters are sampled at $l = 4$ equally spaced levels within their ranges (e.g. inter-particle friction, P_3, is discretized at levels 0.05, 0.33, 0.62, 0.90). A brief survey of the parameters considered as uncertain in this study is presented below to provide the reader more in-depth perspective on the parameters themselves and the rationale for their selection.

Normal spring stiffness (particle-particle P_1 and particle-wall P_2)

Choice of the normal spring stiffness k_n (and k_{nw}) critically affects the computational tractability of CFD-DEM simulations, also shown later in Section 6.3. This is because reducing k_n increases the collision contact time (Eq.(8)) which allows for higher DEM time-step and speeds-up simulations. However, artificially low values of k_n implicitly allow for exceedingly high particle deformations which have adverse implications on the accuracy of simulations. In fact, based on material properties and restrictions on the maximum overlap (0.1–1.0% of particle diameter), very high values of spring stiffness ~$O(10^6 - 10^7$ N/m) are recommended [30, 82]. These are seldom used in practice, however, because of the prohibitive simulation cost even for very small scale systems. On the other hand, there is evidence in literature that as long as k_n is sufficiently high, the precise value (order of magnitude) does not make much difference to predictions [38, 42, 45]. Therefore, in order to cover wide range in particle contact times, the inter-particle normal spring stiffness k_n is chosen as 10^{P_1}, where P_1 is sampled at four uniformly-spaced levels: 1.00, 1.67, 2.32, 3.00 corresponding to $k_n = 10.0$, 46.4, 215.4 and 1000.0 N/m, respectively (and similarly for particle-wall normal stiffness). For this study, the upper limit is set at 1000 N/m in order to ensure computational feasibility and this choice also ensures that almost all collisions (>99.999%) are within the acceptable limit of 1% particle deformation (discussed in Section 6.3).

Friction coefficient (particle-particle P_3 and particle-wall P_4)

The friction coefficient μ depends on both surface roughness as well as sliding velocities of particles. μ values in the range 0.05–0.90 have been measured experimentally [31, 83, 84] and are often considered for sensitivity studies of CFD-DEM simulations (e.g. [36, 38–40, 85, 86]).

Normal restitution (particle-particle P_5 and particle-wall P_6)

Most CFD-DEM simulation studies employ high normal restitution coefficients ($e_n \geq 0.9$) even though experimental measurements indicate that, in addition to material properties, this parameter depends on the impact velocity of two particles: collisions at higher velocities are characterized by lower restitution [87, 88]. The recovered kinetic energy also decreases significantly in the presence of liquid loading (e.g. humidity) because of the formation of bridges between particles [89, 90].

Tangential-normal spring stiffness ratio (particle-particle P_7 and particle-wall P_8)

Due to the difficulties in measurement of tangential impact properties, these are often estimated based on different analytical and semi-empirical approaches. Tangential-normal spring stiffness ratio k_t/k_n depends on the structural properties and is approximately 2/3 for most materials [38]. Shafer et al. [91] proposed 2/7 by conserving time-periods of spring oscillations along the normal and tangential directions for ideal uniform spheres. Deen et al. [27] recommended using $2/7(\pi^2 + ln^2 e_t)/(\pi^2 + ln^2 e_n)$ based on energy balance criteria of dissipative particle, although the determination of tangential restitution e_t itself is challenging [31]. Nevertheless, these two expressions yield similar values for nominal choices of e_n and e_t and are within the bounds of k_t/k_n considered in this study.

Tangential-normal damping ratio (particle-particle P_9 and particle-wall P_{10})

Compared to other model coefficients, the choice of tangential damping coefficient η_t has received significantly less attention. Deen et al. [27] suggested that, similar to η_n Eq.(10), η_t is related to the tangential restitution and spring stiffness coefficients. Based on their recommendation, the ratio η_t/η_n can be simplified to $2/7(ln\ e_t/\ ln\ e_n)$, which is higher than 1 for commonly considered values of tangential restitution coefficient ($e_t \sim 0.3$). Silbert et al. [38] reported minor differences as η_t/η_n was increased from 0 to 1: the system kinetic energy decreased by 8% as more energy was drained out through rotational damping. Based on their recommendations, the default choice of this parameter in MFiX CFD-DEM simulations is 0.5 [86].

DEM time-steps for resolving collisions (P_{11})

The characteristic collision time-scale is $C\sqrt{m_e/k_n}$, where different constants of proportionality have been prescribed previously (e.g. 2 by Cundall and Strack [28], 2π by Tsuji et al. [92]). Particle collisions are typically resolved in 5–50 time-steps, although the exact choice could have significant impact on energy conservation and numerical stability [93]. In MFiX, the collision time between all particles is resolved in 50 time-steps [86].

Tolerance for fluid equations. (P_{12})

At the end of each solver iteration, the sum of residuals for each discretized conservation equation are computed and used as the solution convergence criterion. Lower choice of tolerance values, therefore, ensure more accurate computations but also increase time-to-solution for simulations. The default tolerance in MFiX is 10^{-3}.

DEM-fluid grid interpolation width (P_{13})

Different methods have been proposed for distributing the solids volume fraction onto the fluid grid for interphase (drag) coupling, such as the divided particle-volume and diffusion-based methods [17, 94–96]. For this study, the former is employed which distributes the particle volume over adjoining cells based on the DEM-fluid grid interpolation width: zero-width corresponds to the widely used particle centroid method (whereby the entire particle volume is considered if its centroid lies within a fluid cell) while higher values smoothen the solids fraction distribution over several fluid-cells but require excessive

computation. Overall, this parameter is recommended in the range [d_p, $2\Delta x$], where d_p is the particle diameter and Δx is the fluid-cell dimension [86].

3.3. Assumptions

Model parameters considered for screening analysis pertain largely to particle contacts. The analysis does not consider uncertainties in operating conditions, other sub-models and interactions, as well as the numerical framework (such as spatial or temporal discretization). Some of these are:

- Gas-solid drag model: In this study, the Gidaspow drag model is employed since it is based on measurements in packed and homogeneously fluidized beds. This model has been used extensively in the literature for both Two-Fluid Model and CFD-DEM simulations, and has been previously shown to yield satisfactory predictions for the fluidization of Geldart B particles at low superficial gas flows (see [62] and references therein). However, for applications where the choice of drag model is critical (for instance, circulating fluidization), the statistical framework must include uncertainty in its choice, in addition to other CFD-DEM model parameters.
- Integration schemes: Because of its computational efficiency and lower memory requirements, simulations presented here make use of first order time-integration (default in MFiX). However, comparison of integration schemes is not trivial for multiple simultaneous contacts, especially in the presence of damping, and its choice is often less critical than the use of proper soft models [97, 98]
- Operating conditions: Particle properties, superficial flow profile and bed geometry are chosen to produce alternating pattern in bubble flow. Since pulsating fluidized beds oscillate between regimes dominated by bubble rise and granular relaxation, it is likely that conclusions from this study are applicable to both freely bubbling beds as well as granular flows. Nevertheless, the framework described here can be easily extended to other applications.

Validating these working assumptions and quantifying their impact are outside the scope of this work and will be investigated in more detail in subsequent studies.

4. Simulation setup

Schematic illustration of the rectangular fluidized bed is shown in Fig. 1. The fluidized bed consists of a plenum section, a porous steal plate and a bed of glass beads (of diameter 400 μm and density of 2500 kg/m ^{3}). Air velocity at the inlet of the plenum (3 mm wide) is varied sinusoidally as $U_{in} = 3.40 + 1.80\,sin\,(2\pi ft)$ m/s, where frequency f = 5 Hz. The porous steal plate with thickness 3 mm and permeability $2.68 \times 10^{-12}\ m^2$ acts as a distributor plate with sufficient pressure drop so that the inlet velocity at the bottom of the bed (post-distributor) U_{pd} is spatially uniform and approximately corresponds to

$$U_{pd}/U_{mf} = 1.3 + 0.7\ \ sin(2\pi ft) \tag{18}$$

where $U_{mf} = 0.15$ m/s is the minimum fluidization velocity of glass beads. The thin 5.0×0.5 cm^2 cross-sectional area accommodates 166,380 glass bead particles with static bed height of 3.8 cm. Design and operation of the fluidized bed, including the porous steal plate, particle properties and gas flow profile are chosen to produce repeatable, alternating bubbling patterns, such as those visualized through images captured by a high-speed camera in Fig. 2. The relatively small geometric setup and reasonable particle count makes this setup well suited for both CFD-DEM simulations and laboratory experimentation.

All CFD-DEM simulations are conducted in 3D in order to resolve wall effects in the span-wise direction and to ensure particle coordination profiles similar to those encountered in the experiments. The spatial fluid-grid resolution is 1 mm (2.5 particle diameters) in all dimensions and is based on grid resolution study of the geometry shown in Fig. 1. We conducted simulations using 32×100×4 (coarse grid), 50×160×5 (medium grid) and 64×200×6 (fine grid) cells and Fig. 3 shows that differences in the medium and fine grid predictions are small (compared to differences attributed directly to the choice of model parameters, see Section 6). Governing equations for the gas-phase are solved using the SIMPLE (Semi-Implicit Method for Pressure Linked Equations) algorithm based on finite-volume formulation. The forward Euler approach is used for time marching with adaptive time stepping to maintain numerical stability, typically in the range $10^{-6} - 10^{-3}$s. For the particle (DEM) phase, first-order time-integration is performed with sufficiently low time-step in order to resolve particle collisions (this time-scale depends on both the normal spring stiffness as well as the number of time-steps specified for resolving these collisions). Interphase drag forces are computed by interpolating the gas-phase velocity at particle locations using a second-order Lagrange polynomial. Further details regarding the numerical procedure can be found in [69, 86]. All simulations are conducted for 40s of real time and output data is sampled at 50 Hz frequency, discarding the first 10s for transient start-up effects. In order to accelerate the computational speed, simulations are conducted in parallel and 40–80 cores are dedicated for each simulation.

5. Quantities of interest

Bakshi et al. [99] showed that solids mixing is dependent on size and spatial distributions of the bubbles. However, in the pulsating bed under consideration, the bed dynamics are dominated by alternating bubble rise and granular relaxation mechanisms as the superficial gas flow

Table 1
Model parameters considered for sensitivity analysis of CFD-DEM simulations of gas-solid pulsating fluidized beds. p-p and p-w represent particle-particle and particle-wall collision parameters, respectively.

Label	Model parameter			Range		
	Physical representation	Symbol	Units	Nominal	Min.	Max.
P_1	normal spring stiffness p-p (10^{P_1})	k_n	[N/m]	2.00	1.00	3.00
P_2	normal spring stiffness p-w (10^{P_2})	k_{nw}	[N/m]	2.00	1.00	3.00
P_3	friction coefficient p-p	μ	–	0.30	0.05	0.90
P_4	friction coefficient p-w	μ_w	–	0.30	0.05	0.90
P_5	normal restitution p-p	e_n	–	0.90	0.50	0.98
P_6	normal restitution p-w	e_{nw}	–	0.90	0.50	0.98
P_7	tangential-normal stiffness ratio p-p	k_t/k_n	–	0.29	0.10	0.90
P_8	tangential-normal stiffness ratio p-w	k_{tw}/k_{nw}	–	0.29	0.10	0.90
P_9	tangential-normal damping ratio p-p	η_t/η_n	–	0.50	0.10	0.90
P_{10}	tangential-normal damping ratio p-w	η_{tw}/η_{nw}	–	0.50	0.10	0.90
P_{11}	collision-DEM time-step ratio	τ_{col}/τ_{dem}	–	50	20	50
P_{12}	fluid equations tolerance ($10^{P_{12}}$)		–	−4.00	−6.00	−3.00
P_{13}	DEM-fluid grid interpolation width		[d_p]	2.00	1.00	2.50

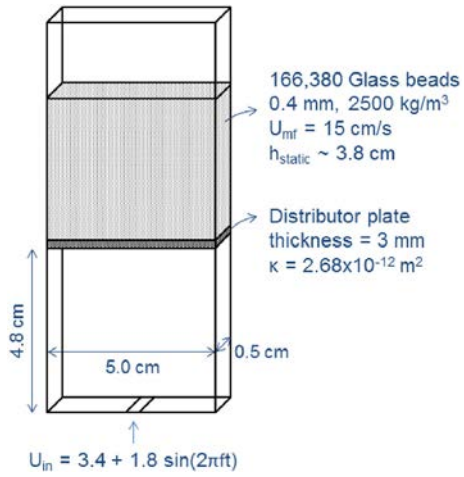

Fig. 1. Schematic of the simulated fluidized bed. Inlet plenum gas flow is varied sinusoidally with frequency f = 5 Hz. Spatial fluid-grid resolution is 1 mm (=2.5×particle diameter) in all directions.

oscillates sinusoidally between 2.0 U_{mf} and 0.6 U_{mf}. Therefore, several Quantities of Interest (QoI): bubble diameter, bubble lateral location, solid particle root mean square velocity and average bed height are selected to appropriately represent the bubbling and solids dynamics in the bed.

5.1. Bubbling dynamics

Bubble detection and tracking are carried out using the software toolkit Multiphase-flow Statistics using 3D Detection and Tracking Algorithm (MS3DATA). MS3DATA detects bubbles efficiently using time-and spatially-resolved simulation data and tracks each bubble based on its trajectory (history) as it rises through the bed. This toolkit is based on MATLAB and can be applied to 2D and 3D fluidized bed simulations. MS3DATA has been validated extensively in [65] and is available open-source at [100].

For all simulations conducted in this study, bubbles are detected using void fraction data along the central vertical axis of the thin rectangular setup (midway between the front and back walls). Threshold for bubble detection ε_{gb} is 0.7 i.e. any pocket of gas with voidage $>\varepsilon_{gb}$ is classified as a bubble [101]. Subsequently, its diameter d_b is calculated using its area A_b i.e. $d_b = \sqrt{4A_b/\pi}$ alongwith other properties such as centroid coordinates, bounding box, aspect ratio and so on. Bubbles smaller than 4 simulation grid cells (i.e. d_b<4 mm) as well as long, flat bubbles close to the distributor (voidage waves typically spanning more than half the cross-section) are discarded. Finally, the average diameter $\overline{d}_b$ is computed using bubble areas, i.e.

$$\overline{d}_b = \sqrt{\frac{\sum d_b^2}{n_b}} \tag{19}$$

where n_b is the total number of bubbles detected. Similarly, average distance of bubbles from the bed center $\overline{x}_b$ is calculated using

$$\overline{x}_b = \frac{\sum |x_b|}{n_b} \tag{20}$$

where bubble lateral location $x_b \in [-W/2, W/2]$ (bed width W = 5 cm). Therefore, relatively high values of $\overline{x}_b$ denote the presence of bubble close to the side walls and are indicative of alternating patterns in bubble flow (verified visually).

5.2. Solids metrics

The particle root mean square velocity vs, rms is calculated using the kinetic energy of all particles in the entire bed i.e.

$$v_{s,rms} = \sqrt{\frac{2\,KE_t}{m n_p}} \quad \text{where} \quad KE_t = \sum_i^{n_p} \frac{1}{2} m v_i^2 \tag{21}$$

where m is the mass and n_p is the total number of particles in the system (= 166,380). Similarly, the average particle height h_s is computed using the potential energy of all particles and simplifies to

$$h_s = \sum_i^{n_p} h_i / n_p \tag{22}$$

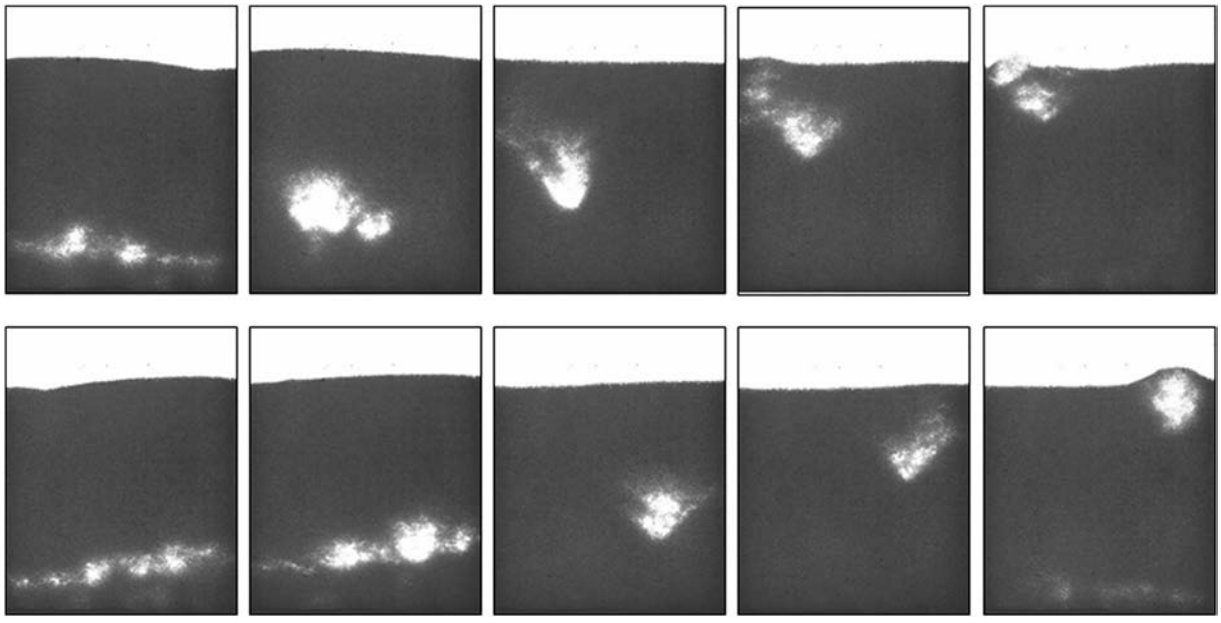

Fig. 2. Sample visualizations of alternating bubble patterns obtained in pulsating fluidization experiments of glass beds. The schematic for these experiments is as shown in Fig. 1 and images are recorded using a high-speed camera at 100 Hz.

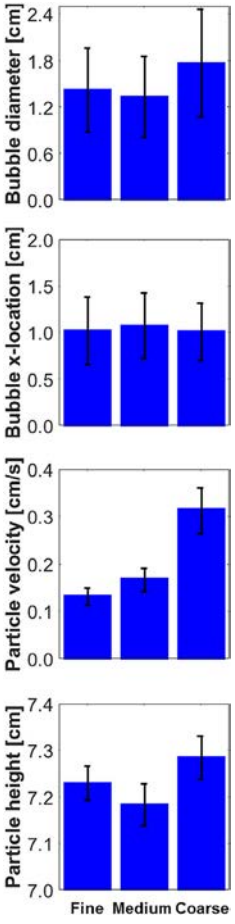

Fig. 3. Effect of grid resolution on the QoIs. Fine grid corresponds to 64 × 200 × 6 cells, medium grid corresponds to 50 × 160 × 5 cells and coarse grid corresponds to 32 × 100 × 4 cells. Error bars indicate standard deviation.

Angular velocity is not considered in this study because rotational energy of particles is insignificant compared to their kinetic energy.

6. Results and discussion

To assess the relative importance of all 13 parameters listed in Table 1, a design matrix with 20 replications was setup using PSUADE (each replication consists of 14 samples). As an illustration, the first replication is presented in Table 2. 3D CFD-DEM simulations are conducted at every sampled point in the parametric space, one replication at a time until statistical convergence is achieved (Section 6.2). Every simulation is conducted for 40s of real time, field data is sampled at 50 Hz frequency and all four QoIs (Section 5) are evaluated over the last 30s. Although a rule of thumb for MOAT analysis is that 10 replications ensure statistical convergence, it is important to note that the required number of samples for any sensitivity analysis is application-specific and depends on the complexity of interactions between the parameters considered. A 20 replication design matrix, therefore, allowed for numerical experimentation until statistical convergence was obtained and avoided redundancies in sampling space (for the current system, 14 replications are deemed sufficient, see Section 6.2).

For model parameters at their nominal values, Fig. 4 shows typical alternating patterns in bubble flow observed in CFD-DEM simulations: a bubble erupts close to the left wall at phase $\phi_1 = 0.8\pi$ and in the subsequent cycle (i.e. $\phi_2 = \phi_1 + 2\pi$), a similar-sized bubble erupts in vicinity of the right wall. Note that ϕ corresponds to the phase of plenum inlet gas flow and the phase-lag of bubble formation (approximately $1.0 - 1.5\pi$ for all cases) corresponds to the residence time for gas-flow through the plenum and porous distributor. Meanwhile, pattern formation is strongly dependent on the choice of model parameters. Instantaneous visualizations of simulations conducted at four samples in the parametric space (picked from the first four replications) are shown in Fig. 5, and clearly demonstrate significant differences in bubble size and spatial distributions arising from the choices of CFD-DEM model parameters. For instance, in runs 15 and 29, bubbles decay rapidly, while run 43 shows large bubbles rising predominantly through the bed center. These observations are consistent with Fig. 6, which shows detailed phase-dependent statistics averaged over the last 30s. While runs 1 and 43 show similar sized bubbles ($\bar{d}_b$ within 8%), the former has significantly higher bubble flow (bubble count n_b is 1.5× higher) which propels faster solids mixing (high rms velocity) as well as higher average bed height because particles are driven upwards as bubbles rise. Overall, these differences in bubbling regimes, their transition, and the expansion and relaxation of bulk solids are attributed directly to the choice of model parameters. Identifying critical particle-scale interactions which affect bubble formation and patterns is key towards unraveling the complexity of gas-solid pulsating fluidization and is only possible through multivariate sensitivity analysis.

6.1. Time averaging

Fig. 7 shows comparison of bubbling and solids dynamic metrics computed using different time-averaging windows. All statistics are phase- and spatially- averaged. For all simulations, patterns are established within 5–10s, corresponding to 25–50 sinusoidal cycles of

Table 2
First replication in the design matrix constructed using MOAT sampling: the first sample is randomly selected and subsequent samples are obtained changing one factor at a time. Parameters P_1—P_{13} alongwith their ranges are defined in Table 1.

#	P_1	P_2	P_3	P_4	P_5	P_6	P_7	P_8	P_9	P_{10}	P_{11}	P_{12}	P_{13}
1	2.33	1.00	0.33	0.05	0.66	0.98	0.63	0.10	0.90	0.63	30	−3.0	0.80
2	2.33	1.00	0.33	0.05	0.66	0.98	0.63	0.10	0.90	0.63	50	−3.0	0.80
3	2.33	1.00	0.33	0.05	0.66	0.98	0.63	0.63	0.90	0.63	50	−3.0	0.80
4	2.33	1.00	0.33	0.05	0.66	0.66	0.63	0.63	0.90	0.63	50	−3.0	0.80
5	2.33	1.00	0.90	0.05	0.66	0.66	0.63	0.63	0.90	0.63	50	−3.0	0.80
6	2.33	1.00	0.90	0.05	0.66	0.66	0.10	0.63	0.90	0.63	50	−3.0	0.80
7	2.33	1.00	0.90	0.05	0.66	0.66	0.10	0.63	0.90	0.63	50	−3.0	0.40
8	2.33	1.00	0.90	0.05	0.66	0.66	0.10	0.63	0.37	0.63	50	−3.0	0.40
9	2.33	1.00	0.90	0.05	0.66	0.66	0.10	0.63	0.37	0.63	50	−5.0	0.40
10	2.33	1.00	0.90	0.62	0.66	0.66	0.10	0.63	0.37	0.63	50	−5.0	0.40
11	2.33	2.33	0.90	0.62	0.66	0.66	0.10	0.63	0.37	0.63	50	−5.0	0.40
12	1.00	2.33	0.90	0.62	0.66	0.66	0.10	0.63	0.37	0.63	50	−5.0	0.40
13	1.00	2.33	0.90	0.62	0.66	0.66	0.10	0.63	0.37	0.10	50	−5.0	0.40
14	1.00	2.33	0.90	0.62	0.98	0.66	0.10	0.63	0.37	0.10	50	−5.0	0.40

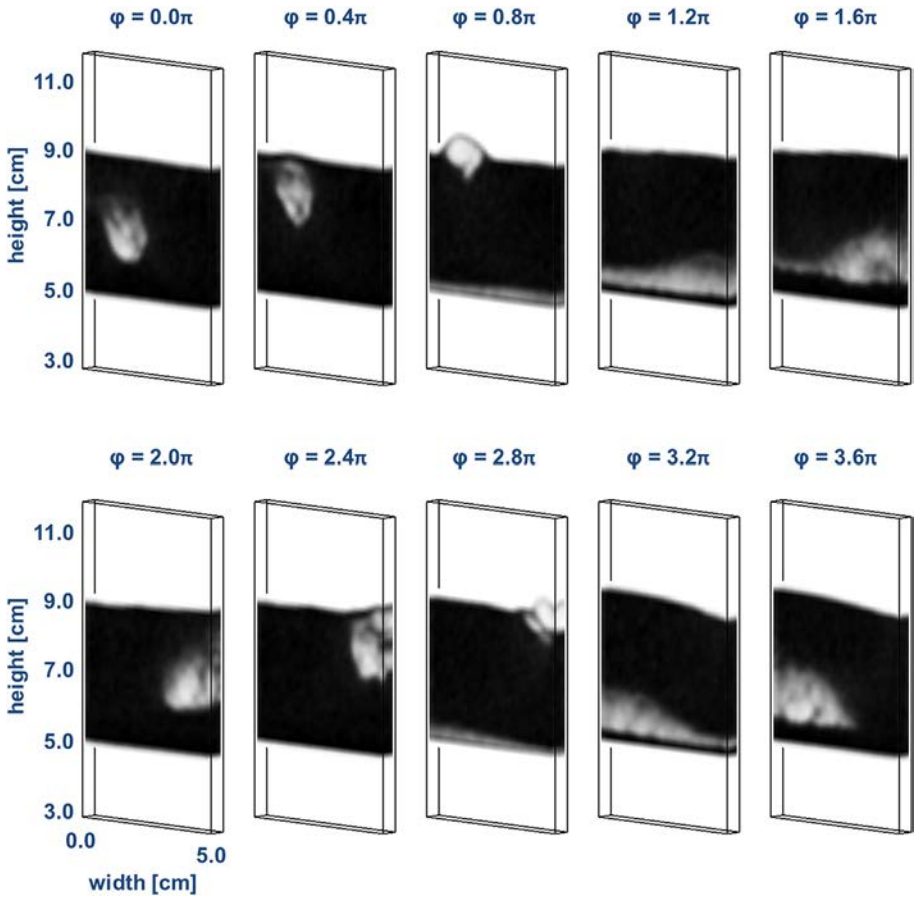

Fig. 4. Visualizations of bubble patterns in 3D CFD-DEM simulations of the pulsating fluidization of 0.4 mm glass beads. ϕ corresponds to phase of plenum inlet gas flow $U_{in} = 3.4 + 1.8\ sin\ (2\pi ft)$ where frequency f = 5 Hz. Model parameters are set at their nominal values (Table 1).

inlet gas flow. These transient start-up effects are also reflected through time-averaging in Fig. 7. Meanwhile, standard deviations in these QoI are invariant to the choice of time-averaging window and their high values (upto 50%) are not surprising because all metrics are averaged over phase and space. Nevertheless, all QoIs show convergence as the time-averaging window is increased from 10–20s to 10–40s and any variations are insignificant compared to differences arising from the choices of model parameters for these simulations. Thus, all simulation data recorded for the first 10s is discarded and only the last 30s are considered for MOAT screening analysis.

It is noteworthy that even though the average bubble diameters in simulation runs 1 and 43 are similar (within 8%), their lateral locations are significantly different: on average, bubbles in simulation run 43 are much closer to the bed center ($\bar{x}_b = 1.10$ cm) than those in run 1 ($\bar{x}_b = 1.56$ cm). Conversely, other simulations not presented here show comparable lateral locations of bubbles but disparate diameters and/or particle velocities. These observations corroborate the need for multiple, independent QoIs for comprehensive sensitivity analysis.

6.2. MOAT analysis

MOAT analysis uses modified means μ^* and standard deviation σ of gradients as sensitivity metrics for identifying critical parameters. Since this method relies on random sampling, it is essential to ensure that the parametric space is sufficiently sampled and captures all nonlinear and coupled interactions. Sample independence for MOAT analysis is checked by observing the convergence of parametric ranking with increasing replications. This procedure is presented for the average bubble diameter in Fig. 8. First, CFD-DEM simulations are conducted for the first $r = 8$ replications (i.e. 112 simulations) and importance ranking of parameters is established using the MOAT metric μ^*. In this case, it is evident that the inter-particle normal restitution P_5, friction P_3, tangential-normal damping ratio P_9 and particle-wall normal restitution P_6 have the strongest influence on bubble sizes. As more replications are simulated ($r = 10$, 12 and 14), the top four significant parameters converge and the fifth ranked parameter, particle-wall friction P_4 is significantly less influential (>4× difference in μ^*) as compared to P_3. In general, minimum sample size requirements of MOAT analysis depend strongly on the system complexity as well as QoI under investigation, although rule of thumb estimates recommend at least 10 replications [71]. In this study, for all QoIs investigated, sensitive parameters are identified within 8 replications (112 simulations), while their rankings converge after 12 replications. Thus, all statistics presented hereafter are based on data from 14 replications (196 simulations).

Fig. 9 shows modified means μ^* (overall influence) and standard deviation σ (interaction effects) of gradients. The closer parameters are to the top right corner, the more influence they have on QoIs. Fig. 9 shows that although all four QoIs are sensitive to P_5, P_3, P_9 and P_6, there are other uncertain parameters with varying degrees of ranking that can effect the gas-phase and solids hydrodynamics. As an example, P_1, P_4 have comparable influence on solids velocities as P_9, although the effect on other QoIs is not as prominent. Meanwhile, the predicted hydrodynamics are relatively insensitive to the tangential-normal spring stiffness ratios (P_7 and P_8), wall parameters (barring P_6) and model-specific numerical parameters P_{11}—P_{13}. Thus, these parameters can be estimated safely based on commonly accepted guidelines. It is important to note that MOAT sensitivity analysis is comparative (i.e. a parameter's importance is gauged relative to the most sensitive ones)

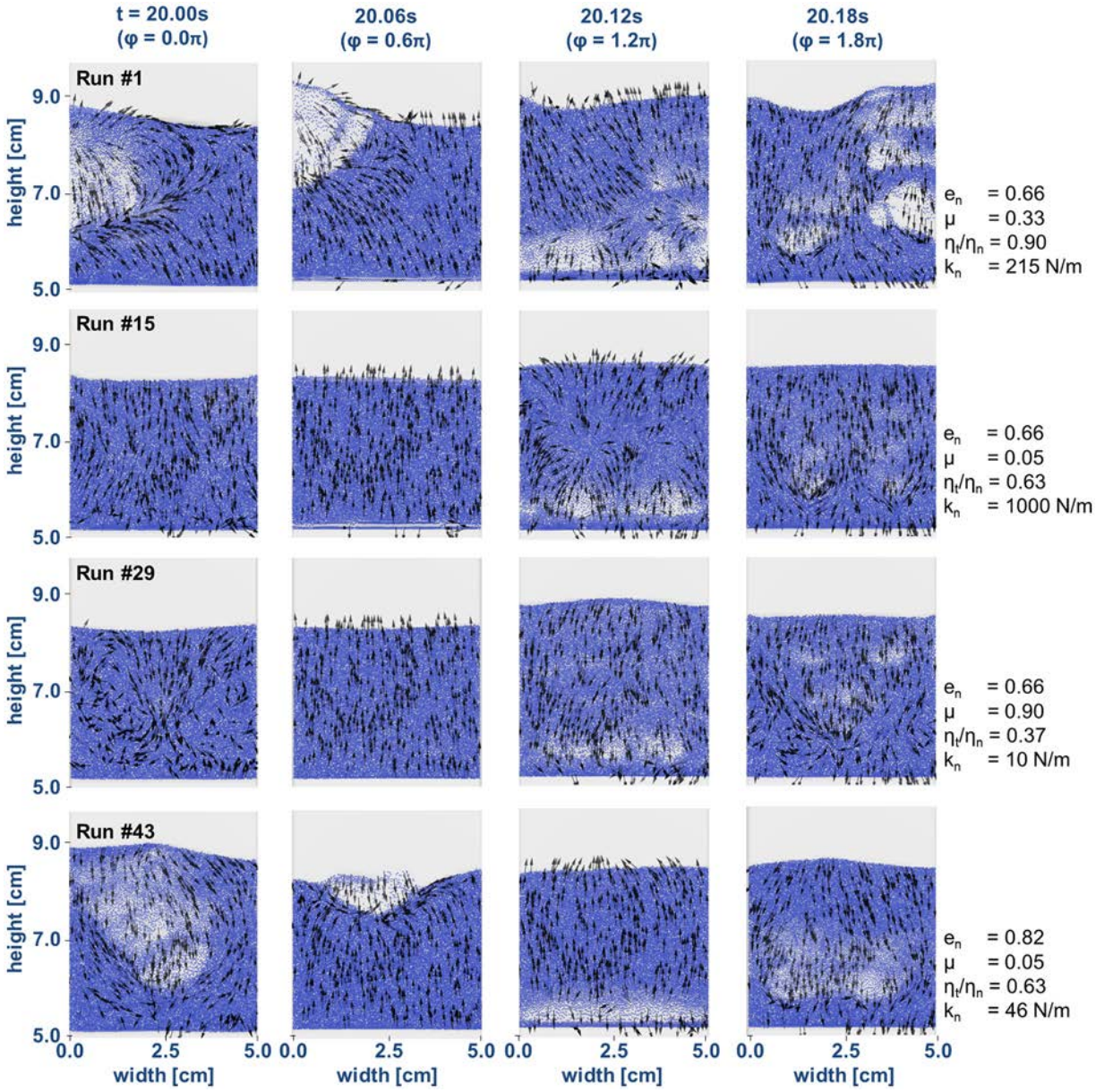

Fig. 5. Bubbling dynamics (overlayed with particle velocity vectors) predicted along the central vertical slice in 3D CFD-DEM simulations. Simulation runs 1, 15, 29 and 43 are picked from the first four replications for MOAT analysis and key model parameters for each simulation are listed on the right. ϕ corresponds to phase of plenum inlet gas flow $U_{in} = 3.4 + 1.8\ sin\ (2\pi ft)$ where frequency f = 5 Hz.

and rankings are specific to parametric ranges considered (Table 1). In the following sections, the impact of critical contact parameters identified using MOAT analysis, i.e. normal spring stiffness, friction, normal restitution and tangential-normal damping ratio, is investigated in more detail.

6.3. Normal spring stiffness

The choice of normal spring stiffness k_n is critical for the computational tractability of CFD-DEM simulations because the time-step for particle motion is inversely proportional to $P_{11}\sqrt{k_n}$. Indeed, Fig. 10 shows that simulations employing k_n=10 N/m are almost 5× faster than those with k_n=1000 N/m. Therefore, low values of k_n are popularly employed in CFD-DEM studies, even though material properties prescribe values in the range 10^6-10^7 N/m. In Fig. 11, the variation in QoIs: bubble diameter and solid rms velocity, is presented, segregating all simulation data points based on their normal spring stiffness (10.0, 46.4, 215.4 and 1000.0 N/m). Fig. 11 shows no visible influence of k_n on bubble diameter predictions, which is consistent with its low importance rank in Fig. 9a as well as previous observations in literature [41–43]. However, particle velocities show significantly high scatter at k_n = 10 N/m. This is because at exceedingly low values of spring stiffness (such as k_n=10 N/m), unphysically high particle contact times and deformations are permitted, both factors amplifying the impact of other contact parameters significantly.

In order to isolate the impact of k_n, we conducted additional simulations with all model parameters at their nominal values in Table 1, except k_n which is varied from 10 to 1000 N/m. Consistent with observations in Fig. 11, Fig. 12 shows that most metrics are insensitive to its choice, but particle velocities increase by almost 25% as k_n is reduced from 1000 to 10 N/m. This apparent discrepancy can be explained using detailed statistics presented in Figs. 13 and 14.In Fig. 13, the distribution of contact deformations is constructed using particle location data from 10 randomly selected time-instances and clearly show

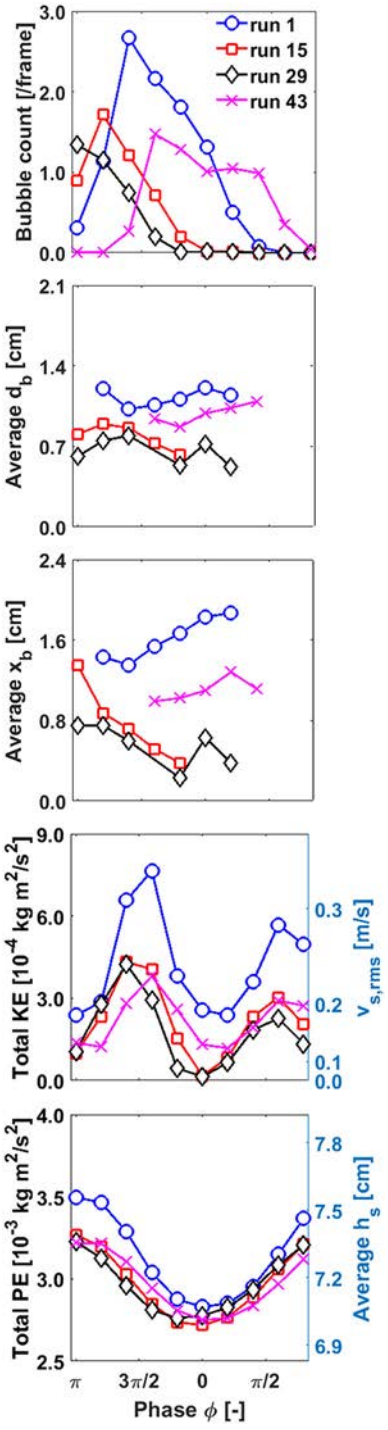

Fig. 6. Phase-dependent variation of bubbling and solids dynamic metrics in 3D CFD-DEM simulations presented in Fig. 5. All statistics are time- and space-averaged over 10s - 40s and ϕ corresponds to phase of plenum inlet gas flow $U_{in} = 3.4 + 1.8\ sin\ (2\pi ft)$ where frequency f = 5 Hz.

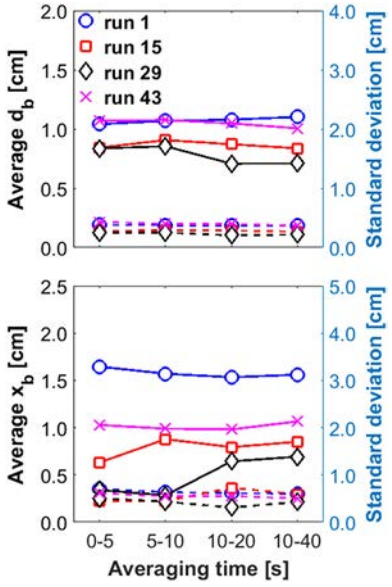

Fig. 7. Impact of time-averaging window on bubbling dynamics in 3D CFD-DEM simulations presented in Fig. 5. Full lines correspond to average values (left y-axis) and dashed lines correspond to standard deviations (right y-axis). All statistics are phase- and space-averaged.

increase in particle overlaps as k_n is reduced; for k_n=1000 N/m, all deformations are within 1% of particle radius while for k_n=10 N/m, almost 0.1% contacts correspond to unphysically high deformations (>5%). This has severe implications particularly within the dense phase because high permitted deformations result in solids over-packing. Fig. 14 shows that during typical instances of bubble rise in simulations employing k_n=10 N/m, majority of the dense phase has solids packing fraction higher than 0.62 (voidage of 0.38), while values in excess of 0.70 are not uncommon. Such compaction is physically unreasonable, considering that random loose packing of monodisperse spheres is typically 0.60 [102]. This over-compaction of the dense phase reduces its permeability for gas-flow which promotes faster bubble rise [101], analogous to the observation of *fast bubbles* in the fluidization of Geldart A particles (verified through visualizations, but accurate quantification is difficult because of significant deformations as bubbles form and rise in shallow beds). Consequently, faster bubbles drive faster solids mixing [99], explaining the observation of higher particle rms velocities at lower k_n.

6.3.1. k_n-independent solution

To check dependence of hydrodynamic predictions on k_n when relatively high values are chosen, additional MOAT analysis is conducted using the top six parameters identified in Fig. 9: restitution coefficients P_5 (p-p: particle-particle) and P_6 (p-w: particle-wall), friction coefficients P_3 (p-p) and P_4 (p-w), tangential-normal damping ratio P_9 (p-p) and normal spring stiffness P_1 (p-p). For this analysis, k_n which is chosen in the range [100, 1000] N/m (i.e. exceedingly low values of k_n are not considered) while ranges for P_3—P_6, P_9 are identical to those considered in Fig. 9 and all other model parameters are selected at their nominal values in Table 1. Fig. 15 shows modified means and standard deviations based on $r = 10$ replications (7 simulations per replication). Parametric sensitivities differ considerably from those presented in Fig. 9: for instance, Fig. 15 shows that bubble sizes are affected predominantly by the choice of normal restitution, unlike Fig. 9 which shows comparable influence of friction and tangential-normal damping ratio. More notably, the influence of normal spring stiffness is insignificant (order of magnitude of μ^* is lower than that for most critical parameters), which suggests that its precise value is not crucial within the considered range. This is consistent with observations in literature suggesting that beyond a critical value, the choice of k_n has no impact on the predicted hydrodynamics, and is explained in more detail below.

6.3.2. Optimal choice of normal spring stiffness

Most guidelines on the choice of spring stiffness are based on particle-overlap and impact velocity considerations in a binary collision (e.g. [32, 93]), but do not account for macroscopic (bubbling/cluster)

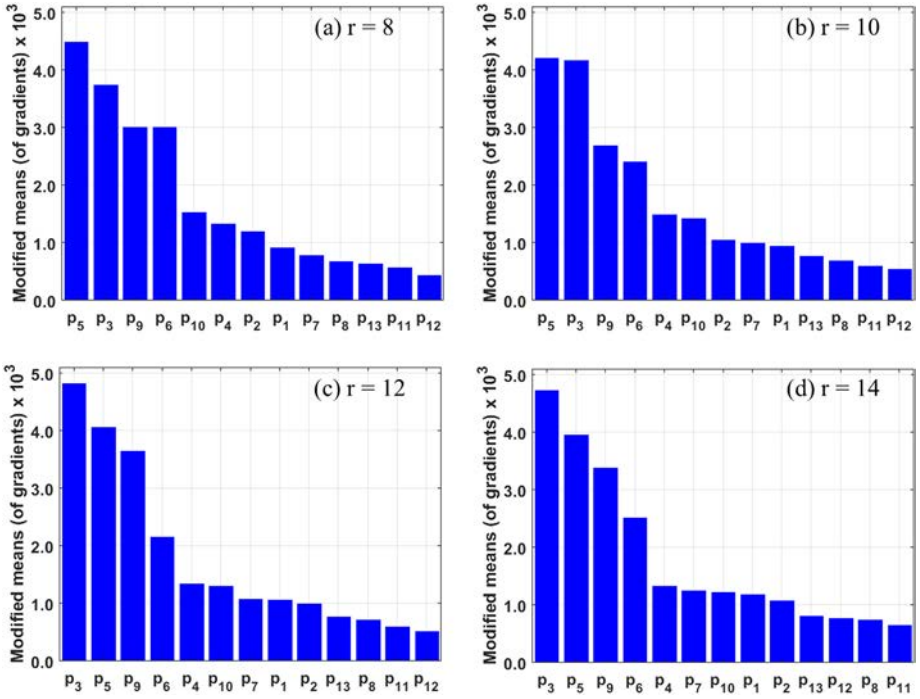

Fig. 8. MOAT sensitivity analysis of average bubble diameter in 3D CFD-DEM simulations. Input model parameters $P_1 \ldots P_{13}$ (Table 1) are ranked in order of decreasing sensitivity. One replication corresponds to 14 simulations and increasing replications ($r = 8$, 10, 12 and 14) are considered for demonstrating statistical convergence.

dynamics. These guidelines are likely to be over-stringent for many gas-solid flow applications where inter-phase momentum exchange and reactor-scale transport significantly influence particle coordination and contact times. In order to determine the optimal choice of k_n, the ratio of particle relaxation and collision time-scales is considered below.

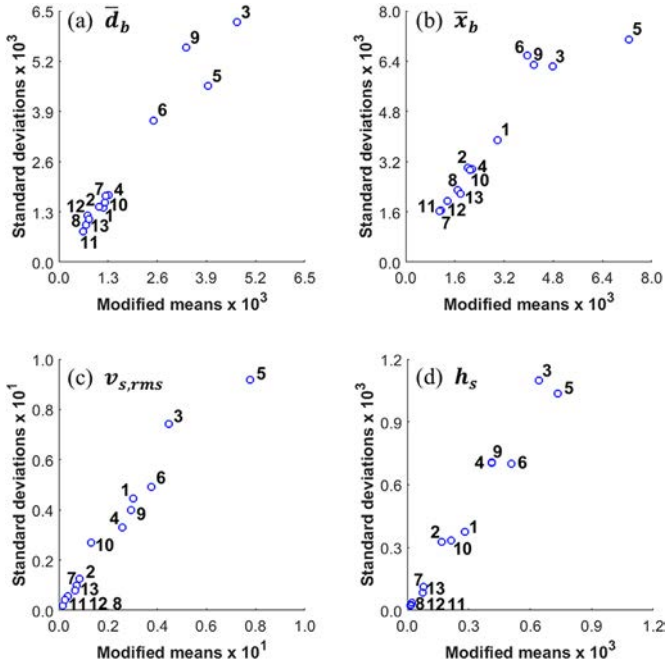

Fig. 9. MOAT sensitivity analysis of all quantities of interest in 3D CFD-DEM simulations, using $r = 14$ replications. Input model parameters $P_1 \ldots P_{13}$ (Table 1) are ranked based on modified means and standard deviations of gradients and those closer to top-right corner have higher sensitivities.

Assuming the free-fall of a particle under solids pressure P_s over distance d_p, the particle relaxation (inertia) time-scale is

$$t_p = \frac{d_p}{\sqrt{P_s/\rho_p}} \tag{23}$$

where d_p and ρ_p are the particle diameter and density, respectively. Close to bubble boundaries, particle collisions dominate over enduring contacts and the kinetic theory of granular flow [68] is applicable, so that

$$P_s = \rho_s \theta_s (1 + 2(1 + e_n) g_0 \varepsilon_s) \tag{24}$$

$$g_0 = \left(1 - \left(\frac{\varepsilon_s}{\varepsilon_{s,\,max}}\right)^{1/3}\right)^{-1}$$

where ε_s is the solids volume fraction and g_0 is the radial distribution function. θ_s is the local granular temperature and since $\theta_s \sim v_s^2$ [68], Eq. (23) can be simplified to

$$t_p = \frac{d_p}{v_s \sqrt{1 + 2(1 + e_n) g_0 \varepsilon_s}} \tag{25}$$

Using the collision time-scale t_{col} in Eq. (8), the ratio t_{col}/t_p for monodisperse spheres is

$$\tilde{t}_{col} = \frac{t_{col}}{t_p} = \left(\sqrt{\frac{\pi d_p \rho_p}{12}}\right)_1 \left(\sqrt{\frac{\pi^2 + \ln^2 e_n}{k_n}}\right)_2 \left(v_s \sqrt{1 + 2(1 + e_n) g_0 \varepsilon_s}\right)_3 \tag{26}$$

which is dependent on particle properties $(\,)_1$, contact parameters $(\,)_2$ and local flow dynamics $(\,)_3$. In reality, $\tilde{t}_{col} << 1$ (because $k_n = 10^6$-10^7 N/m, based on material properties) which suggests that contact time-scale between any two particles is decoupled from their reactor-scale transport. However, if the choice of k_n is such that $\tilde{t}_{col} \sim O(1)$, particle contacts are permitted to be 'sticky' (relative to flow time-scales)

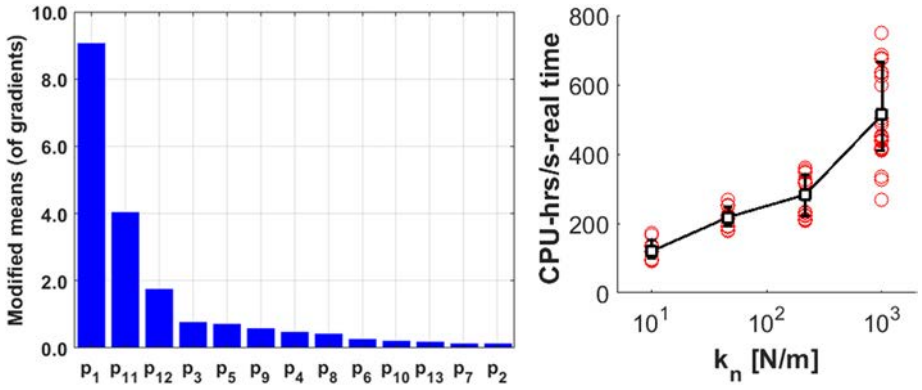

Fig. 10. (left) MOAT sensitivity analysis of computational cost of 3D CFD-DEM simulations. Input model parameters $P_1 \ldots P_{13}$ (Table 1) are ranked in order of decreasing sensitivity. (right) Dependence of computational cost on inter-particle normal spring stiffness k_n. Red circles correspond to 3D CFD-DEM simulation data points and error bars represent standard deviation.

and, therefore, the accuracy of predicted hydrodynamics is compromised. For particles investigated in this system (d_p=0.4 mm, ρ_p= 2500 kg/m ^{3}) with contacts characterized by nominal restitution e_n = 0.9, the dependence of k_n on particle velocity v_s is presented in Fig. 16, for $\bar{t}_{col}$=0.1. This calculation suggests that, as the flow-time scale decreases (v_s increases), k_n must be raised in order to further reduce the collision time between particles. Based on typical solids velocities 10–30 cm/s observed in our pulsating bed simulations, this analysis clearly demonstrates that (a) choosing k_n=10 N/m will result in 'sticky' contacts (relative to flow time-scales) and (b) k_n>100 N/m will ensure that particle contacts are sufficiently decoupled from bulk solids transport (and its precise value thereafter does not matter). Both observations are consistent with analysis presented earlier in this section. Note that calculations in Fig. 16 are based on solids volume fraction ε_s=0.3 in order to investigate the flow-field in the vicinity of bubbles.

Overall, time-scale analysis discussed in this section is valuable for choosing optimal values of k_n so that computations are feasible (which is not possible using k_n=10 ^{6}-10 ^{7} N/m), yet do not permit artificially high contact times which could alter macro-scale dynamics (as with k_n=10 N/m in this study). Further, this analysis can be easily extended to determine k_n in CFD-DEM simulations of circulating fluidized beds (where cluster relaxation dynamics may be important) as well as for modeling more complex phenomena such as adhesion, heat transfer and so on accurately (by accounting for respective time-scales).

6.4. Coupling of dissipation parameters

In this section, we investigate the coupled influence of critical dissipation parameters: normal restitution, friction coefficient and tangential-normal damping ratio using reactor-scale hydrodynamic predictions as well as detailed statistics of particle distribution and flow dynamics. While the dependence of fluidization metrics on restitution and friction coefficients is generally well-recognized, we show that these sensitivities strongly hinge on the relative choices of these parameters. Similarly, the tangential-normal damping ratio has received considerably less attention in CFD-DEM literature, although Figs. 9 and 15 clearly demonstrate its importance to hydrodynamic predictions.

6.4.1. Friction and normal restitution

Fig. 17 shows that both the particle rms velocity and average height increase with bubble size. This is because larger bubbles rise faster, leading to faster solids upflow in their nose and wake regions and faster downflow along the lateral edges as bubbles burst into the freeboard [99]. Fig. 18 shows the combined influence of inter-particle friction and normal restitution coefficients. When particle contacts are near-ideal (i.e. low friction and/or high restitution), the average bubble size, particle rms velocity and average height increase because significantly lower energy is dissipated on particle contacts. On the other hand, highly dissipative contacts result in the rapid decay of bubbles and the bed simply expands and collapses without the propagation of bubbles. These trends are consistent with results reported in literature. However, sensitivity to any parameter hinges on the choice of other

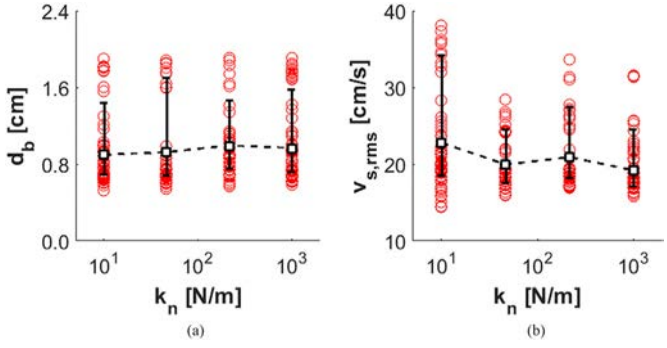

Fig. 11. Dependence of (a) average bubble diameter and (b) particle root mean square velocity on inter-particle normal spring stiffness k_n. Red circles correspond to 3D CFD-DEM simulation data points presented in Section 6.2 and error bars represent standard deviation.

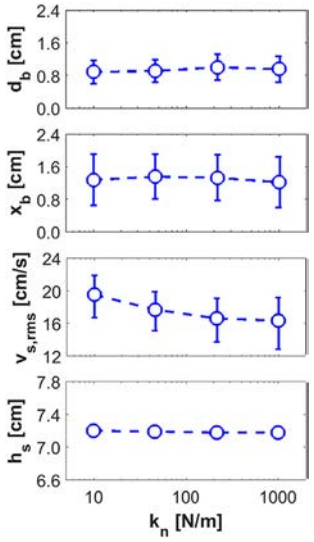

Fig. 12. Dependence of bubbling and solids dynamic metrics on inter-particle normal spring stiffness k_n in 3D CFD-DEM simulations. All input model parameters are set on their nominal values listed in Table 1, except k_n which is varied over 10–1000 N/m. Error bars represent standard deviation.

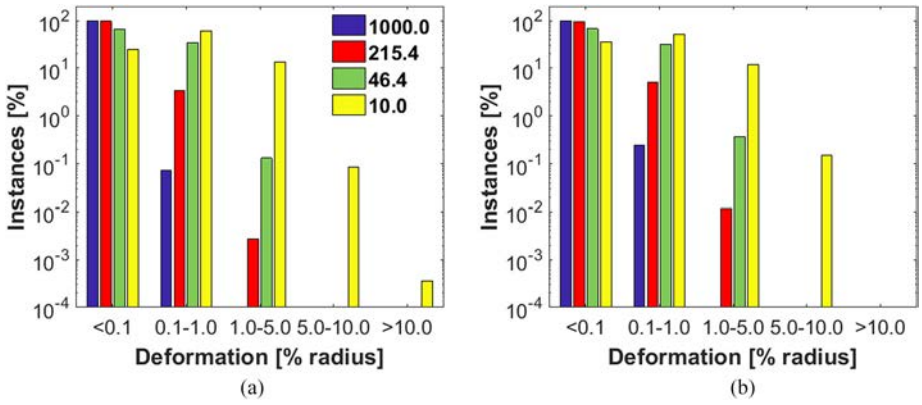

Fig. 13. Dependence of deformation profiles of contacting particles on normal spring stiffness k_n (in legend). Statistics are computed using 10 randomly selected time-instances in 3D CFD-DEM simulations presented in Fig. 12.

dissipation parameters. For instance, results are significantly sensitive to e_n when μ=0.05 (e.g. rms velocity drops by almost 40% when e_n is reduced from 0.98 to 0.50), and are relatively insensitive when high values of μ are chosen (e.g. rms velocity decreases by 10% at $\mu \geq 0.5$). Similar observations can be made about sensitivities to friction at low and high normal restitutions. Meanwhile, bubble lateral locations are indicative of alternating bubbling patterns (such as visualizations shown in Fig. 4) because higher values of $\overline{x}_b$ indicate bubbles in proximity of the side walls. Fig. 18 shows non-monotonic dependence of $\overline{x}_b$ on friction and normal restitution: low dissipation parameters ($\mu = 0.05$ and $e_n \geq 0.8$) result in the formation of large bubbles which rise predominantly through the bed center, while the combination $\mu \geq 0.50$ and $e_n < 0.8$ causes bubbles to decay rapidly. Thus, alternating bubble pattern is stable only under slightly inelastic/frictional particle contacts and ceases to exist at either extremes of the contact dissipation spectrum (also shown in Fig. 19). The stability of patterns and their correlation with particle energy will be analyzed in detail in future studies.

6.4.2. Friction and tangential damping

To examine the interplay between friction and tangential damping, we conducted a series of simulations varying $\mu \in [0.2, 0.4]$ and $\eta_t/\eta_n \in [0.1,0.9]$, with all model parameters kept at their nominal values (Table 1). Note that the normal damping coefficient η_n is identical for all simulations because k_n and e_n are fixed at 100 N/m and 0.9, respectively (see Eq. (10)). Statistics from these simulations are presented in Fig. 20 and all simulations predict bubble patterns and QoI (diameter, x-location) similar to the base case ($\mu = 0.3, \eta_t/\eta_n = 0.5$). Careful examination of the particle dynamics, however, reveals interesting insights into the coupling of friction and tangential-normal damping ratio. We performed detailed calculations of particle location and velocity data extracted from 10 randomly-selected time instants, and segregated statistics in different sections of the bed. Fig. 21 presents the particle rms velocities, average coordination numbers and slip velocities and their dependence on local void fraction. For the i^{th} particle, the coordination number N_c^i is the number of particles it is in contact with, while its average slip velocity $V^i_{s,\,slip}$ is given by

$$V^i_{s,slip} = \frac{1}{N_c^i}\sum_j^{N_p} \; | \boldsymbol{V}^i - \boldsymbol{V}^j | \, \delta_{ij} \; and \; N_c^i = \sum_j^{N_p} \delta_{ij} \tag{27}$$

$$where \; \delta_{ij} = \begin{cases} 1, & \text{if } | X^i - X^j | \; < d_p \text{ and } \; i \neq j \\ 0, & \text{otherwise} \end{cases}$$

Fig. 21 shows that as voidage increases, the average coordination number first decreases as particle packing decreases, and then increases indicating the formation of small clusters as particles accelerate/rain down inside rising bubbles. Meanwhile, the average particle slip

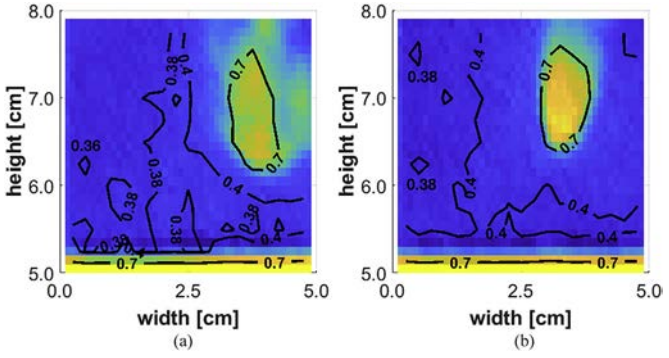

Fig. 14. Distribution of void fraction (with contours) at typical instants of bubbling in 3D CFD-DEM simulations with inter-particle normal spring stiffness k_n= 10 and 1000 N/m. All other parameters are set at their nominal values in Table 1.

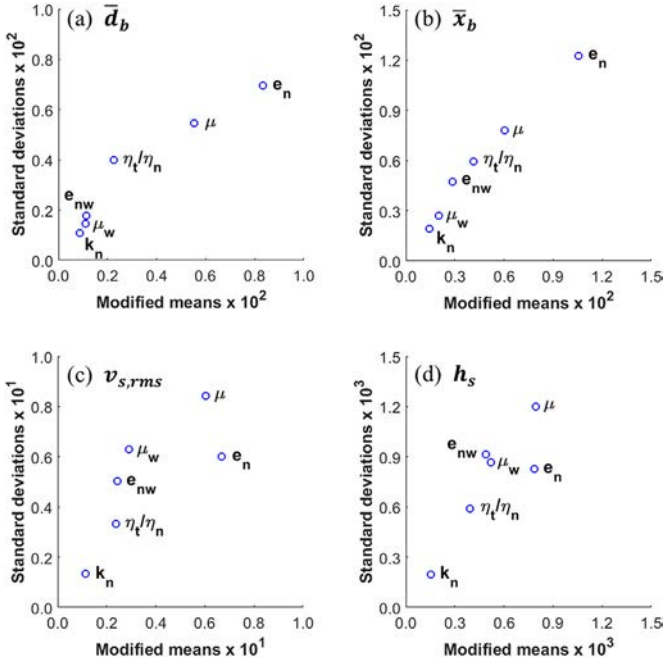

Fig. 15. MOAT sensitivity analysis of top 6 parameters identified in Fig. 9, using $r = 10$ replications. Normal spring stiffness $k_n \in [100,1000]$ N/m while ranges for all other input parameters are as listed in Table 1. Parameters are ranked based on modified means and standard deviations of gradients and those closer to top-right corner have higher sensitivities.

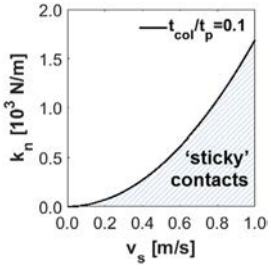

Fig. 16. Dependence of normal spring stiffness k_n on particle velocity v_s based on comparison of particle collision t_{col} and relaxation t_p time scales (Eq. (25)).

velocity varies inversely with the coordination number which is expected because increasing particle contacts result in higher dissipative interactions, thereby, reducing the former.

Fig. 21 also demonstrates that in highly dense areas of the bed ($\varepsilon_g < 0.6$): (a) particle rms velocities increase at higher voidage because of lower coordination; and (b) the sensitivity of dynamics to changes in μ and η_t/η_n are minimal because particles are closely packed and their dynamics are dependent largely on the bulk (expansion and relaxation) solids motion [99]. More importantly, in areas occupied by bubbles, distinct differences are seen: simulations with relatively high dissipation parameters (μ=0.3, η_t/η_n=0.9 and μ=0.4, η_t/η_n=0.5) have significantly lower particle rms velocities as compared to the others. This observation can be explained by examining the average coordination numbers and particle slip velocities within dilute pockets of the bed ($\varepsilon_g \in [0.7,0.9]$) as presented in Fig. 22. Here, the x-axis is scaled as $\mu\eta_t/\eta_n$ which represents the product of frictional and tangential spring forces, both non-dimensionalized by the normal spring force. Fig. 22 distinctly demonstrates that as μ or η_t/η_n are increased, particle coordination increases and their slip velocities reduce, both observations suggesting the higher tendency of particles to cluster.

Meanwhile, slip velocity statistics presented in Fig. 23 demonstrate the coupled influence of friction coefficient and tangential-normal damping ratio on average slip velocities: at $\eta_t/\eta_n = 0.1$, slip velocities decrease by almost 50% (from 1.59 cm/s to 0.85 cm/s) as μ increases from 0.2 to 0.4 (similar observation when η_t/η_n is increased from 0.1 to 0.9, at μ=0.2). This is unlike the case at $\eta_t/\eta_n = 0.9$, where average slip velocities are relatively low (0.6–0.7 cm/s) and are insensitive to

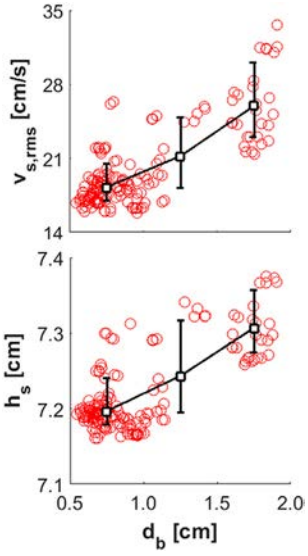

Fig. 17. Dependence of particle rms velocity and average height on average bubble diameter. Red circles correspond to 3D CFD-DEM simulation data points presented in Section 6.2 and error bars represent standard deviation.

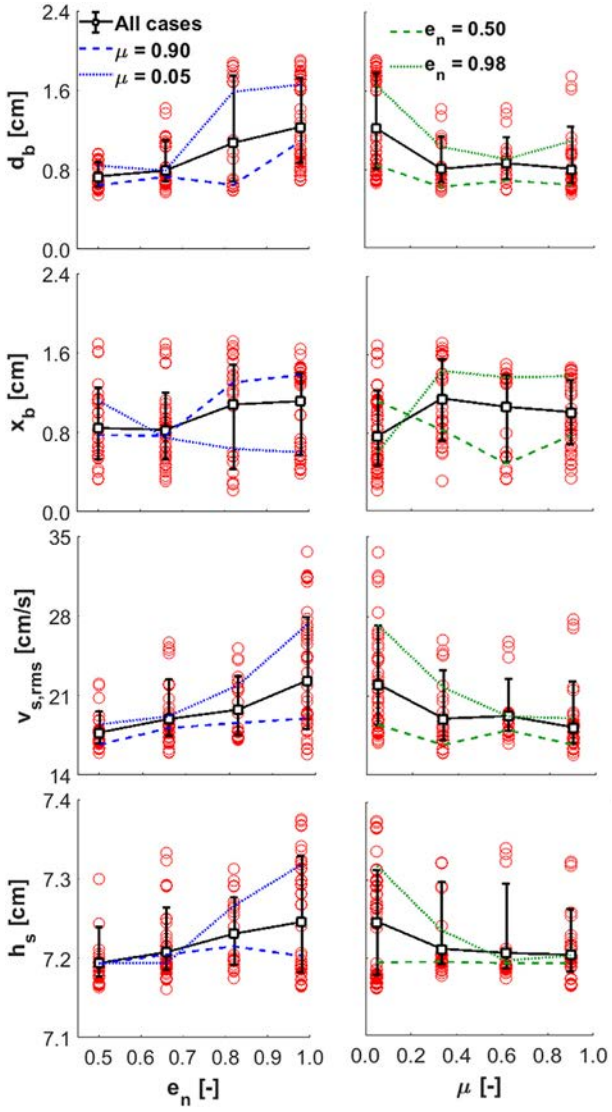

Fig. 18. Dependence of bubbling and particle dynamic metrics on inter-particle normal restitution e_n and friction μ. Red circles correspond to 3D CFD-DEM simulation data points presented in Section 6.2 (except those which employ k_n = 10 N/m) and error bars represent standard deviation.

the choice of μ. Thus, similar to the coupled influence of normal restitution and friction on bubbling dynamics (Section 6.4.1), the sensitivity of particle dynamics to friction μ hinges on the choice of η_t/η_n. Based on observations in Figs. 22 and 23 it follows that as η_t/η_n is increased, particles dissipate higher tangential momentum on contact, reducing their slip velocities and making the choice of μ less relevant. Similarly, the reverse sensitivity is also true: simulations are significantly more sensitive to η_t/η_n when dissipation through other sources (friction and normal restitution coefficients) is minimal.

Overall, the analysis conducted in this section elucidates the coupled influence of friction and tangential damping, even though these model parameters operate in different ways mechanistically: friction acts as a switch for sliding/no-sliding of particles (and, therefore, alters the tangential spring force in Eq. (11), while the latter is a direct sink for tangential momentum as particles contact. This coupling makes parameter estimation and model calibration extremely challenging. However, observations in Figs. 21–23 suggest that particle velocity measurements under conditions of dilute solids loading could provide suitable datasets for validating models for tangential damping and will be investigated in subsequent studies.

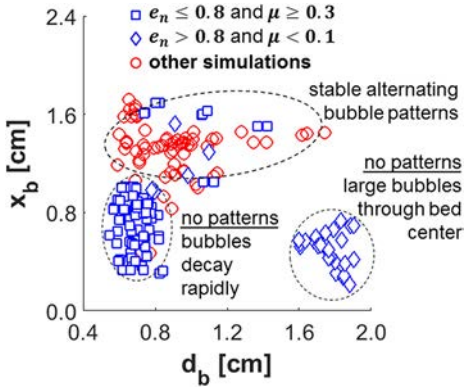

Fig. 19. Average diameter d_b and lateral distance of bubbles from bed center x_b for pulsating bed simulations. e_n and μ are the normal restitution and friction coefficients, respectively. Larger values of x_b indicate higher likelihood of bubbling patterns.

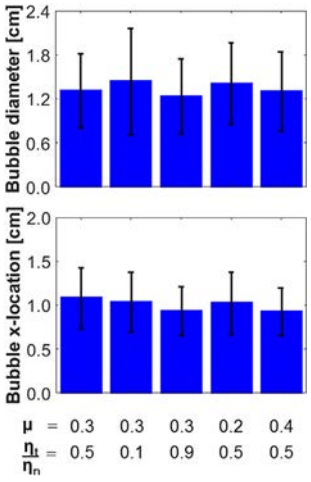

Fig. 20. Bubble statistics (diameter and x-location) in simulations with different choices of inter-particle friction μ and tangential-normal damping ratio η_t/η_n. All other input model parameters are set at their nominal values prescribed in Table 1. Error bars represent standard deviation.

7. Conclusion

CFD-DEM simulations are employed in a wide range of multiphysics, multiscale applications for the fundamental investigation of particle-scale phenomena as well as for the development and validation of reduced fidelity models. There is considerable uncertainty in the selection of model parameters because experimental measurements are largely restricted to binary normal collisions of particles. In this study, we employ multivariate sensitivity analysis to identify critical model parameters in the CFD-DEM simulations of fluidized beds and quantify their impact on gas-solid flow hydrodynamics. Towards this end, a total of 13 model (and model-specific numerical) parameters are identified based on a survey of existing literature and feedback from domain experts. Next, a sampling design matrix is constructed based on the Morris-One-At-a-Time (MOAT) approach and 3D CFD-DEM simulations are conducted for the application to a pulsating fluidized bed. Based on detailed bubble and particle dynamics metrics from 250+ simulations, we identify the normal spring-stiffness, normal restitution, friction and tangential damping coefficients as the key parameters impacting fluidization hydrodynamics. Next, we quantify their coupled impact and investigate fundamentally the mechanism through which these critical parameters impact hydrodynamic predictions, using detailed statistics of particle distribution and flow dynamics.

In order to increase the computational time-step (and hence, speed-up simulations), low values of normal spring stiffness k_n are popularly employed, even though material properties prescribe values in the range 10^6-10^7 N/m. While choosing k_n as low as 10 N/m has no visible impact on bubble size and spatial distributions (in the shallow bed simulations conducted in this study), simulations show significant impact on particle dynamics. This is because unrealistically high particle deformations (>10% of particle radius) are permitted at exceedingly low k_n. Unphysically high compaction of the dense-phase results in faster bubble flow and solids mixing around bubbles. Based on these observations, a working expression for optimally choosing k_n is proposed which ensures that the time-scale for particle contacts is sufficiently decoupled from granular relaxation (flow) time-scales, as bubbles rise. For the dense fluidization of glass beads considered in this study, we show that the choice of k_n=100 N/m satisfies this criterion and ensures that almost all particle contacts have acceptable (<1%) deformation. The proposed correlation is dependent on particle

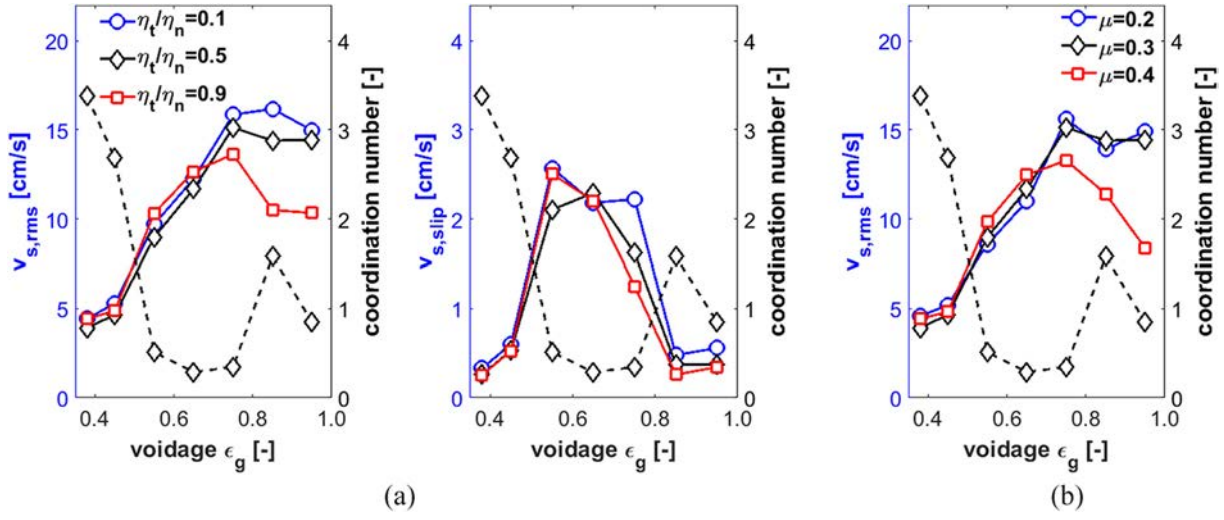

Fig. 21. Particle rms and average slip velocities (solid lines) (a) at constant friction coefficient μ=0.3 and tangential-normal damping ratio η_t/η_n=0.1, 0.5 and 0.9, and (b) at constant η_t/η_n=0.5 and μ=0.2, 0.3 and 0.4. Average particle coordination numbers (dashed line) are plotted for the simulation employing μ=0.3 and η_t/η_n=0.5. All other CFD-DEM model parameters are chosen at their nominal values in Table 1 and statistics are computed using particle location and velocity data from 10 randomly-selected time-instants.

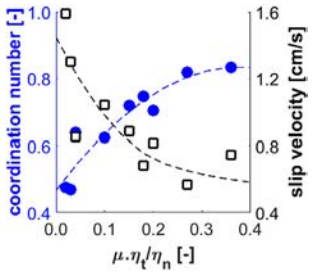

Fig. 22. Average coordination numbers (blue filled circles) and particle slip velocities (black hollow squares) in dilute pockets of the bed $\varepsilon_g \in [0.7,0.9]$ computed in all simulations with friction coefficient μ=0.2, 0.3 and 0.4 and tangential-normal damping ratio η_t/η_n=0.1, 0.5 and 0.9. All other CFD-DEM model parameters are chosen at their nominal values in Table 1 and statistics are computed using particle location and velocity data from 10 randomly-selected time-instants.

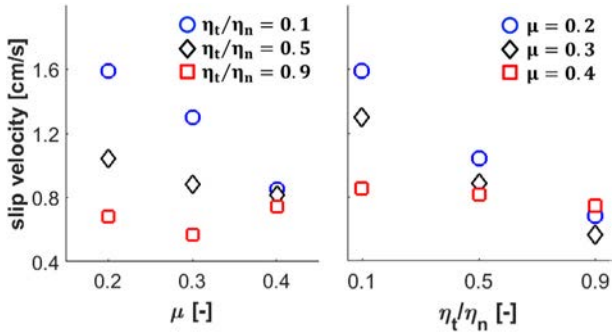

Fig. 23. Dependence of average particle slip velocity on the choice of friction coefficient μ and tangential-normal damping ratio η_t/η_n, in dilute pockets of the bed $\varepsilon_g \in [0.7,0.9]$. All other CFD-DEM model parameters are chosen at their nominal values in Table 1 and statistics are computed using particle location and velocity data from 10 randomly-selected time-instants.

properties, contact parameters and local flow dynamics (solids distribution and velocity) around bubbles, and the framework can be extended easily to other applications of CFD-DEM simulations.

Next, we show that the influence of dissipation parameters is strongly coupled. For instance, as the normal restitution coefficient is increased, larger bubbles and higher particle velocities are observed because less energy is dissipated during particle contacts. However, this sensitivity decreases as the inter-particle friction is raised. Similarly, friction plays a much more prominent role at higher values of normal restitution. On the other hand, tangential damping could significantly influence particle dynamics: detailed flow-field statistics clearly demonstrate that in dilute regions of the bed, both friction and tangential damping have comparable influence on particle coordination, slip velocities and overall dynamics. Overall, the combination of these dissipation parameters affects the stability of bubble patterns in pulsating beds: patterns break down in simulations where: (a) particle collisions are almost-elastic (large bubbles rise predominantly through the bed center) or (b) contact parameters are very dissipative causing bubbles to decay rapidly after formation.

This is one of the first studies where large-scale parametric analysis is conducted to investigate several CFD-DEM model parameters simultaneously; in total, 250+ 3D simulations are conducted with almost 170,000 glass particles each. Our observations strongly suggest that comprehensive sensitivity analysis of dynamic systems such as fluidized beds is only possible if (a) all relevant model parameters are considered in a quantitative manner through methods like Morris-One-At-A-Time (MOAT) screening, so that the analysis is not susceptible to bias with respect to fixed choices of other parameters, and (b) multiple, independent dynamic metrics are considered, in order to ensure that the underlying physics are completely characterized. Findings in this study provide important guidelines for the selection of model parameters as well as for the design of experiments to validate them. Although focused on bubble pattern formation in a small-scale pulsating fluidized beds, it is likely that conclusions drawn from this study are applicable to larger-scale simulations of granular, freely bubbling and/or other gas-solid systems which exhibit similar underlying particle collision dynamics and their coupling with reactor-scale flow heterogeneities. More importantly, the statistical framework developed here for screening and analysis of computationally expensive simulations provides a robust strategy for the fundamental investigation of other particle-scale phenomena (such as cohesion, adhesion, sintering, liquid bridging and so on) as well as for simulation-based reactor design and optimization.

Acknowledgment

This technical effort was performed in support of the National Energy Technology Laboratory (NETL) ongoing research under the RES contract DE-FE0004000, and supported in part by an appointment to the National Energy Technology Laboratory Research Participation Program, sponsored by the U.S. Department of Energy and administered by the Oak Ridge Institute for Science and Education.

Disclaimer

References

[1] D. Kunii, O. Levenspiel, Fluidization Engineering, 1991.
[2] S. Pannala, M. Syamlal, T.J. O'Brien, Computational Gas-Solids Flows and Reacting Systems: Theory, Methods and Practice, IGI Global, 2011.
[3] D.C. Miller, D.S. Mebane M. Syamlal, C. Storlie, D. Bhattacharyya, N.V. Sahinidis, D. Agarwal, C. Tong, S.E. Zitney, A. Sarkar, X. Sun, S. Sundaresan, E. Ryan, D. Engel, C. Dale, Carbon capture simulation initiative: a case study in multiscale modeling and new challenges, Annu. Rev. Chem. Biomol. Eng. 5 (2014) 301–323.
[4] N.P. Siegel, C.K. Ho, S.S. Khalsa, and G.J. Kolb. Development and evaluation of a prototype solid particle receiver: on-sun testing and model validation. ASME. J. Sol. Energy Eng., 132(2):021008–021008–8, 2010.
[5] M.A. van der Hoef, M. van Sint Annaland, N.G. Deen, J.A.M. Kuipers, Numerical simulation of dense gas-solid fluidized beds: a multiscale modeling strategy, Annu. Rev. Fluid Mech. 40 (2008) 47–70.
[6] P. Liu, C.M. Hrenya, Challenges of dem: I. Competing bottlenecks in parallelization of gas–solid flows, Powder Technol. 264 (2014) 620–626.
[7] A.V. Patil, E.A.J.F. Peters, J.A.M. Kuipers, Comparison of CFD-DEM heat transfer simulations with infrared/visual measurements, Chem. Eng. J. 277 (2015) 388–401.
[8] A.B. Morris, Z. Ma, S. Pannala, C.M. Hrenya, Simulations of heat transfer to solid particles flowing through an array of heated tubes, Sol. Energy 130 (2016) 101–115.
[9] C. M. Boyce, A. Ozel, J. Kolehmainen, and S. Sundaresan. Analysis of the effect of small amounts of liquid on gas–solid fluidization using CFD-DEM simulations. AICHE J.
[10] L. Lu, B. Gopalan, S. Benyahia, Assessment of different discrete particle methods ability to predict gas-particle flow in a small-scale fluidized bed, Ind. Eng. Chem. Res. 56 (27) (2017) 7865–7876.
[11] L. Lu, A. Morris, T. Li, S. Benyahia, Extension of a coarse grained particle method to simulate heat transfer in fluidized beds, Int. J. Heat Mass Transf. 111 (2017) 723–735.
[12] T. Tsuji, K. Yabumoto, T. Tanaka, Spontaneous structures in three-dimensional bubbling gas-fluidized bed by parallel demcfd coupling simulation, Powder Technol. 184 (2) (2008) 132–140.

[13] N. Gui, J.R. Fan, K. Luo, DEM-LES study of 3-d bubbling fluidized bed with immersed tubes, Chem. Eng. Sci. 63 (14) (2008) 3654–3663.
[14] A.E.C. Varas, E.A.J.F. Peters, J.A.M. Kuipers, Cfd-dem simulations and experimental validation of clustering phenomena and riser hydrodynamics, Chem. Eng. Sci. 169 (2017) 246–258.
[15] D. Jajcevic, E. Siegmann, C. Radeke, J.G. Khinast, Large-scale CFD-DEM simulations of fluidized granular systems, Chem. Eng. Sci. 98 (2013) 298–310.
[16] M. Saidi, H.B. Tabrizi, J.R. Grace, C.J. Lim, Hydrodynamic investigation of gas-solid flow in rectangular spout-fluid bed using CFD-DEM modeling, Powder Technol. 284 (2015) 355–364.
[17] J. Capecelatro, O. Desjardins, An Euler-Lagrange strategy for simulating particle-laden flows, J. Comput. Phys. 238 (2013) 1–31.
[18] M. Fang, K. Luo, S. Yang, K. Zhang, J. Fan, Computational fluid dynamics-discrete element method investigation of solid mixing characteristics in an internally circulating fluidized bed, Ind. Eng. Chem. Res. 52 (22) (2013) 7556–7568.
[19] P. Pepiot, O. Desjardins, Numerical analysis of the dynamics of two- and three-dimensional fluidized bed reactors using an EulerLagrange approach, Powder Technol. 220 (2012) 104–121.
[20] O. Oke, B. Van Wachem, L. Mazzei, Lateral solid mixing in gas-fluidized beds: CFD and DEM studies, Chem. Eng. Res. Des. 114 (2016) 148–161.
[21] B. Krause, B. Liedmann, J. Wiese, P. Bucher, S. Wirtz, H. Piringer, V. Scherer, 3D DEM-CFD simulation of heat and mass transfer, gas combustion and calcination in an intermittent operating lime shaft kiln, Int. J. Therm. Sci. 117 (2017) 121–135.
[22] X. Ku, T. Li, T. Løvås, CFD-DEM simulation of biomass gasification with steam in a fluidized bed reactor, Chem. Eng. Sci. 122 (2015) 270–283.
[23] Y. Li, W. Ji, Acceleration of coupled granular flow and fluid flow simulations in pebble bed energy systems, Nucl. Eng. Des. 258 (2013) 275–283.
[24] J. Zhao, T. Shan, Coupled cfdddem simulation of fluidparticle interaction in geomechanics, Powder Technol. 239 (2013) 248–258.
[25] H. Yu, W. Cheng, L. Wu, H. Wang, Y. Xie, Mechanisms of dust diffuse pollution under forced-exhaust ventilation in fully-mechanized excavation faces by cfd-dem, Powder Technol. 317 (2017) 31–47.
[26] F. Qian, N. Huang, J. Lu, Y. Han, dem simulation of the filtration performance for fibrous media based on the mimic structure, Comput. Chem. Eng. 71 (2014) 478–488.
[27] N.G. Deen, M. Van Sint Annaland, M.A. Van der Hoef, J.A.M. Kuipers, Review of discrete particle modeling of fluidized beds, Chem. Eng. Sci. 62 (1) (2007) 28–44 (Fluidized Bed Applications).
[28] P.A. Cundall, O.D.L. Strack, A discrete numerical model for granular assemblies, Geotechnique 29 (1) (1979) 47–65.
[29] H. Kruggel-Emden, F. Stepanek, A. Munjiza, A study on adjusted contact force laws for accelerated large scale discrete element simulations, Particuology 8 (2) (2010) 161–175.
[30] A. Di Renzo, F.P. Di Maio, Comparison of contact-force models for the simulation of collisions in dem-based granular flow codes, Chem. Eng. Sci. 59 (3) (2004) 525–541.
[31] H. Kruggel-Emden, S. Wirtz, V. Scherer, A study on tangential force laws applicable to the discrete element method (dem) for materials with viscoelastic or plastic behavior, Chem. Eng. Sci. 63 (6) (2008) 1523–1541.
[32] H.A. Navarro, M.P. de Souza Braun, Determination of the normal spring stiffness coefficient in the linear springdashpot contact model of discrete element method, Powder Technol. 246 (2013) 707–722.
[33] Y. He, T. Wang, N. Deen, M. van Sint Annaland, J.A.M. Kuipers, D. Wen, Discrete particle modeling of granular temperature distribution in a bubbling fluidized bed, Particuology 10 (4) (2012) 428–437.
[34] M.S. van Buijtenen, N.G. Deen, S. Heinrich, S. Antonyuk, J.A.M. Kuipers, Discrete particle simulation study on the influence of the restitution coefficient on spout fluidized-bed dynamics, Chem. Eng. Technol. 32 (3) (2009) 454–462.
[35] B.P.B. Hoomans, J.A.M. Kuipers, W.J. Briels, W.P.M. van Swaaij, Discrete particle simulation of bubble and slug formation in a two-dimensional gas-fluidised bed: a hard-sphere approach, Chem. Eng. Sci. 51 (1) (1996) 99–118.
[36] J. Li, J.A.M. Kuipers, Effect of competition between particle “particle and gas” particle interactions on flow patterns in dense gas-fluidized beds, Chem. Eng. Sci. 62 (13) (2007) 3429–3442.
[37] C.R. Muller, S.A. Scott, D.J. Holland, B.C. Clarke, A.J. Sederman, J.S. Dennis, L.F. Gladden, Validation of a discrete element model using magnetic resonance measurements, Particuology 7 (4) (2009) 297–306.
[38] L.E. Silbert, D. Ertas, G.S. Grest, T.C. Halsey, D. Levine, S.J. Plimpton, Granular flow down an inclined plane: Bagnold scaling and rheology, Phys. Rev. E 64 (051302) (2001).
[39] J.W. Wang, M.A. van der Hoef, J.A.M. Kuipers, The role of particle-particle interactions in bubbling gas-fluidized beds of geldart a particles: a discrete particle study, AIP Conf. Proc. 1207 (2010) 766–774.
[40] R. Wilson, D. Dini, B. van Wachem, A numerical study exploring the effect of particle properties on the fluidization of adhesive particles, AICHE J. 62 (5) (2016) 1467–1477.
[41] Y. Kaneko, T. Shiojima, M. Horio, Dem simulation of fluidized beds for gas-phase olefin polymerization, Chem. Eng. Sci. 54 (24) (1999) 5809–5821.
[42] R. Moreno-Atanasio, B.H. Xu, M. Ghadiri, Computer simulation of the effect of contact stiffness and adhesion on the fluidization behaviour of powders, Chem. Eng. Sci. 62 (1) (2007) 184–194.
[43] Y. Gu, A. Ozel, S. Sundaresan, A modified cohesion model for cfddem simulations of fluidization, Powder Technol. 296 (2016) 17–28.
[44] S. Lommen, D. Schott, G. Lodewijks, Dem speedup: stiffness effects on behavior of bulk material, Particuology 12 (2014) 107–112.
[45] M. Paulick, M. Morgeneyer, A. Kwade, Review on the influence of elastic particle properties on dem simulation results, Powder Technol. 283 (2015) 66–76.
[46] A. Gel, R. Garg, C. Tong, M. Shahnam, C. Guenther, Applying uncertainty quantification to multiphase flow computational fluid dynamics, Powder Technol. 242 (2013) 27–39.
[47] A. Gel, M. Shahnam, J. Musser, A.K. Subramaniyan, J.F. Dietiker, Nonintrusive uncertainty quantification of computational fluid dynamics simulations of a bench-scale fluidized-bed gasifier, Ind. Eng. Chem. Res. 55 (48) (2016) 12477–12490.
[48] M. Shahnam, A. Gel, A.K. Subramaniyan J. Dietiker, and J. Musser. The effect of grid resolution and reaction models in simulation of a fluidized bed gasifier through nonintrusive uncertainty quantification techniques. ASME J. Verif. Valid. Uncert., 1(4):041004–041004–9, 2017.
[49] A. Vaidheeswaran, A. Gel, J. Musser, W.A. Rogers, M. Shahnam, Development of verification, validation and uncertainty quantification roadmap with systematic set of validation experiments and simulation campaign, ASME Verification and Validation Symposium, American Society of Mechanical Engineers, 2017.
[50] L. Massimilla, G. Volpicelli, G. Raso, A study on pulsating gas fluidization of beds of particles, Chem. Eng. Prog. Symp. Ser. 62 (1966).
[51] H.W. Wong, M.H.I. Baird, Fluidisation in a pulsed gas flow, Chem. Eng. J. 2 (2) (1971) 104–113.
[52] Murat Köksal, Hüseyin Vural, Bubble size control in a two-dimensional fluidized bed using a moving double plate distributor, Powder Technol. 95 (3) (1998) 205–213.
[53] D. Zhang, M. Köksal, Heat transfer in a pulsed bubbling fluidized bed, Powder Technol. 168 (1) (2006) 21–31.
[54] S.S. Dokka, H. Arastoopour, Simulation of a pulsating bed using eulerian approach, 12th International Conference on FluidizationNew Horizons in Fluidization Engineering 2007, pp. 743–750.
[55] Z. Li, W. Su, Z. Wu, R. Wang, A.S. Mujumdar, Investigation of flow behaviors and bubble characteristics of a pulse fluidized bed via cfd modeling, Dry. Technol. 28 (2009).
[56] A. Miyoshi, T. Kawaguchi, T. Tanaka, Y. Tsuji, Numerical analysis on effects on pulsating gas on flows in gas-solid fluidized bed, Proc. of Fourth International Particle Technology Forum, 2000.
[57] T. Kawaguchi, T.A. Miyoshi, Tanaka, Y. Tsuji, Discrete particle analysis of 2D pulsating fluidized bed, Proc. of 4th Int. Conf. on Multiphase Flow 2001, p. 838.
[58] X.S. Wang, M.J. Rhodes, Pulsed fluidizationa dem study of a fascinating phenomenon, Powder Technol. 159 (3) (2005) 142–149.
[59] M.O. Coppens, C.M. Van den Bleek, M.A. Regelink, Pulsation induced transition from chaos to periodically ordered patterns in fluidized beds, Proceedings of the Fourth World Conference on Particle Technology, Vol. 355, , 2002.
[60] M.O. Coppens and J.R van Ommen. Structuring chaotic fluidized beds. Chem. Eng. J., 96(1):117–124, 2003. Festschrift Prof. Cor M. van den Bleek.
[61] K. Wu, L. de Martin, L. Mazzei, M.O. Coppens, Pattern formation in fluidized beds as a tool for model validation: a two-fluid model based study, Powder Technol. 295 (2016) 35–42.
[62] A. Bakshi, C. Altantzis, A. Bershanska, A.K. Stark, A.F. Ghoniem, On the limitations of 2D CFD for thin-rectangular fluidized bed simulations, Powder Technol. 332 (2018) 114–119.
[63] D.G. de Oliveira, O.O. Ayeni, C.L. Wu, K. Nandakumar, J.B. Joshi, Controlling the flow structure in fluidized bed: a CFD-DEM approach, Proceedings of the 7th International Conference on Discrete Element Methods, 188, 2017, p. 1.
[64] K. Wu, L. de Martin, M.O. Coppens, Pattern formation in pulsed gas-solid fluidized beds –the role of granular solid mechanics, Chem. Eng. J. 329 (2017) 4–14.
[65] A. Bakshi, C. Altantzis, R.B. Bates, A.F. Ghoniem, Multiphase-flow Statistics using 3D Detection and Tracking Algorithm (MS3DATA): methodology and application to large-scale fluidized beds, Chem. Eng. J. 293 (2016) 355–364.
[66] NETL Multiphase Flow Science, MFiX Software Suite, https://mfix.netl.doe.gov/mfix/ 2016.
[67] H.J. Herrmann, S. Luding, Modeling granular media on the computer, Contin. Mech. Thermodyn. 10 (4) (1998) 189–231.
[68] D. Gidaspow, Multiphase Flow and Fluidization: Continuum and Kinetic Theory Descriptions, Academic, Boston, 1994.
[69] R. Garg, J. Galvin, T. Li, S. Pennala, Open-source mfix-dem software for gas solids flows: part i - verification studies, Powder Technol. 220 (2012) 122–137.
[70] T. Li, R. Garg, J. Galvin, S. Pennala, Open-source mfix-dem software for gas solids flows: part ii - validation studies, Powder Technol. 220 (2012) 138–150.
[71] Y. Gan, Q. Duan, W. Gong, C. Tong, Y. Sun, W. Chu, A. Ye, C. Miao, Z. Di, A comprehensive evaluation of various sensitivity analysis methods: a case study with a hydrological model, Environ. Model Softw. 51 (2014) 269–285.
[72] Max D. Morris, Factorial sampling plans for preliminary computational experiments, Technometrics 33 (2) (1991) 161–174.
[73] F. Campolongo, J. Cariboni, A. Saltelli, An effective screening design for sensitivity analysis of large models, Environ. Model Softw. 22 (10) (2007) 1509–1518.
[74] S. Hirabayashi, C.N. Kroll, D.J. Nowak, Component-based development and sensitivity analyses of an air pollutant dry deposition model, Environ. Model Softw. 26 (6) (2011) 804–816.
[75] M.L. Chu-Agor, R. MuÃoz-Carpena, G. Kiker, A. Emanuelsson, I. Linkov, Exploring vulnerability of coastal habitats to sea level rise through global sensitivity andÂ uncertainty analyses, Environ. Model Softw. 26 (5) (2011) 593–604.
[76] J.D. Herman, J.B. Kollat, P.M. Reed, T. Wagener, Technical note: Method of morris effectively reduces the computational demands of global sensitivity analysis for distributed watershed models, Hydrol. Earth Syst. Sci. 17 (7) (2013) 2893.
[77] J. Wu, R. Dhingra, M. Gambhir, J.V. Remais, Sensitivity analysis of infectious disease models: methods, advances and their application, J. R. Soc. Interface 10 (86) (2013).

[78] D. Garcia Sanchez, B. LacarriÃre, M. Musy, B. Bourges, Application of sensitivity analysis in building energy simulations: combining first- and second-order elementary effects methods, Energy Build. 68 (Part C) (2014) 741–750.
[79] P. Heiselberg, H. Brohus, A. Hesselholt, H. Rasmussen, E. Seinre, S. Thomas, Application of sensitivity analysis in design of sustainable buildings, Renew. Energy 34 (2009) 2030–2036.
[80] B. Ciuffo, C.L. Azevedo, A sensitivity-analysis-based approach for the calibration of traffic simulation models, IEEE Trans. Intell. Transp. Syst. 15 (3) (2014) 1298–1309.
[81] Q. Ge, M. Menendez, An efficient sensitivity analysis approach for computationally expensive microscopic traffic simulation models, Int. J. Transp. 2 (2014) 49–64.
[82] P.W. Cleary, DEM simulation of industrial particle flows: case studies of dragline excavators, mixing in tumblers and centrifugal mills, Powder Technol. 109 (1) (2000) 83–104.
[83] S.F. Foerster, M.Y. Louge, H. Chang, K. Allia, Measurements of the collision properties of small spheres, Phys. Fluids 6 (1994) 1108–1115.
[84] A. Lorenz, C. Tuozzolo, M.Y. Louge, Measurements of impact properties of small, nearly spherical particles, Exp. Mech. 37 (3) (Sep 1997) 292–298.
[85] C.Q. LaMarche, P. Liu, K.M. Kellogg, A.W. Weimer, C.M. Hrenya, A system-size independent validation of CFD-DEM for noncohesive particles, AICHE J. 61 (12) (2015) 4051–4058.
[86] T. Li R. Garg, J. Galvin, S. Pannala, Documentation of Open-Source mfixdem Software for Gas-Solids FlowsTechnical report 2012.
[87] A.B. Stevens, C.M. Hrenya, Comparison of soft-sphere models to measurements of collision properties during normal impacts, Powder Technol. 154 (2) (2005) 99–109.
[88] H. Kruggel-Emden, E. Simsek, S. Rickelt, S. Wirtz, V. Scherer, Review and extension of normal force models for the discrete element method, Powder Technol. 171 (3) (2007) 157–173.
[89] J. Fu, M.J. Adams, G.K. Reynolds, A.D. Salman, M.J. Hounslow, Impact deformation and rebound of wet granules, Powder Technol. 140 (3) (2004) 248–257.
[90] V.S. Sutkar, N.G. Deen, J.T. Jenkins, J.A.M. Kuipers, V. Salikov, B. Cruger, S. Antonyuk, S. Heinrich, A novel approach to determine wet restitution coefficients through a unified correlation and energy analysis, AICHE J. 61 (3) (2015) 769–779.
[91] J. Schafer, S. Dippel, D.E. Wolf, Force scheme in simulations of granular materials, J. Phys. 1 France 6 (1) (1996) 5–20.
[92] Y. Tsuji, T. Kawaguchi, T. Tanaka, Discrete particle simulation of two-dimensional fluidized bed, Powder Technol. 77 (1) (1993) 79–87.
[93] K.F. Malone, B.H. Xu, Determination of contact parameters for discrete element method simulations of granular systems, Particuology 6 (6) (2008) 521–528.
[94] C.L. Wu, J.M. Zhan, Y.S. Li, K.S. Lam, A.S. Berrouk, Accurate void fraction calculation for three-dimensional discrete particle model on unstructured mesh, Chem. Eng. Sci. 64 (6) (2009) 1260–1266.
[95] R. Sun, H. Xiao, Diffusion-based coarse graining in hybrid continuumdiscrete solvers: theoretical formulation and a priori tests, Int. J. Multiphase Flow 77 (2015) 142–157.
[96] Z. Peng, E. Doroodchi, C. Luo, B. Moghtaderi, Influence of void fraction calculation on fidelity of CFD-DEM simulation of gas-solid bubbling fluidized beds, AICHE J. 60 (6) (2014) 2000–2018.
[97] H. Kruggel-Emden, F. Stepanek, A. Munjiza, Performance of integration schemes in discrete element simulations of particle systems involving consecutive contacts, Comput. Chem. Eng. 35 (10) (2011) 2152–2157.
[98] K.J. Hanley, C. OSullivan, Analytical study of the accuracy of discrete element simulations, Int. J. Numer. Methods Eng. 109 (2017) 29–51.
[99] A. Bakshi, A.F. Ghoniem, C. Altantzis, Mixing dynamics in bubbling fluidized beds, AICHE J. 63 (10) (2017) 4316–4328.
[100] A. Bakshi, C. Altantzis, R.B. Bates, A. Bershanska, A.F. Ghoniem, Multiphase-flow Statistics using 3D Detection and Tracking Algorithm (MS3DATA) toolkit, https://github.com/akhileshbakshi/MS3DATA-2D 2017.
[101] A. Bakshi, C. Altantzis, L.R. Glicksman, A.F. Ghoniem, Gas-flow distribution in bubbling fluidized beds: CFD-based analysis and impact of operating conditions, Powder Technol. 316 (2017) 500–511 (Fluidization for Emerging Green Technologies).
[102] A.B. Yu, N. Standish, Porosity calculations of multi-component mixtures of spherical particles, Powder Technol. 52 (3) (1987) 233–241.